Integrated Fe and S isotope study of seafloor hydrothermal vents at East Pacific Rise 9-10ºN

Olivier Rouxel[1], Wayne C. Shanks III[2], Wolfgang Bach[1,3] and Katrina J. Edwards[1,4]

[1] Marine Chemistry and Geochemistry Department, Woods Hole Oceanographic Institution, MS#25, Woods Hole, MA 02543, USA

[2] U.S. Geological Survey, 973 Denver Federal Center, Denver, CO 80225, USA

[3] University of Bremen, Geoscience Dept., PO Box 334440. 28359 Bremen, Germany

[4] Department of Biological Sciences, University of Southern California, Los Angeles, CA 90089, USA

In revision to Chemical Geology

Corresponding author
Olivier Rouxel
Woods Hole Oceanographic Institution
Marine Chemistry & Geochemistry Dept., MS#25
Woods Hole, MA 02543
Office: (508) 289-3655
Fax: (508) 457-2013
orouxel@whoi.edu

Keywords: iron isotopes, sulfur isotopes, hydrothermal systems, sulfide deposits

Abstract

In this study, we report on coupled Fe- and S-isotope systematics of hydrothermal fluids and sulfide deposits from the East Pacific Rise at 9-10°N to better constrain processes affecting Fe-isotope fractionation in hydrothermal environments. We aim to address three fundamental questions: (1) is there significant Fe isotope fractionation during sulfide precipitation? (2) Is there significant variability of Fe-isotope composition of the hydrothermal fluids reflecting sulfide precipitation in subsurface environments? (3) Are there any systematics between Fe- and S-isotopes in sulfide minerals? The results show that chalcopyrite, precipitating in the interior wall of a hydrothermal chimney displays a limited range of δ^{56}Fe values and δ^{34}S values, between –0.11 to –0.33‰ and 2.2 to 2.6‰ respectively. The δ^{56}Fe values are, on average, slightly higher by 0.14‰ relative to coeval vent fluid composition while δ^{34}S values suggest significant S-isotope fractionation (-0.6±0.2‰) during chalcopyrite precipitation. In contrast, systematically lower δ^{56}Fe and δ^{34}S values relative to hydrothermal fluids, by up to 0.91‰ and 2.0‰ respectively, are observed in pyrite and marcasite precipitating in the interior of active chimneys. These results suggest isotope disequilibrium in both Fe- and S-isotopes due to S-isotopic exchange between hydrothermal H_2S and seawater SO_4^{2-} followed by rapid formation of pyrite from FeS precursors, thus preserving the effects of a strong kinetic Fe-isotope fractionation during FeS precipitation. In contrast, δ^{56}Fe and δ^{34}S values of pyrite from inactive massive sulfides, which show evidence of extensive late-stage reworking, are essentially similar to the hydrothermal fluids. Multiple stages of remineralization of ancient chimney deposits at the seafloor appear to produce minimal Fe-isotope fractionation. Similar affects are indicated during subsurface sulfide precipitation as demonstrated by the lack of systematic differences between δ^{56}Fe values in both high-temperature, Fe-rich black smokers and lower temperature, Fe-depleted vents.

1. Introduction

Seafloor hydrothermal activity at mid-ocean ridges and ridge-flanks is one of the fundamental processes controlling the exchange of heat and chemical species between seawater and ocean crust (Edmond et al., 1979; Elderfield and Schultz, 1996). Traditionally, the behavior of metals and metalloids in seafloor hydrothermal systems has been investigated by integrating results from laboratory studies, theoretical models, mineralogy, and fluid and mineral chemistry (e.g. Seewald and Seyfried, 1990; Humphris et al., 1995; Tivey, 1995b; Von Damm, 1995). Past studies have demonstrated the complexity and diversity of seafloor hydrothermal systems and have highlighted the importance of subsurface environments in controlling the composition of hydrothermal fluids and mineralization types (e.g., Janecky and Shanks, 1988; Edmond et al., 1995; Hannington et al., 1995; Tivey et al., 1995; Fouquet, 1997). For example, cooling of the hydrothermal fluid and mixing with seawater in subsurface environments are key factors controlling the metal solubility and type of hydrothermal vents, including focused high-temperature (200 to 350°C) outflow through black and white smoker chimneys as well as low-temperature (<50°C) diffuse flow. However, in many cases, the affects of subsurface sulfide precipitation and metal remobilization are difficult to identify based solely on chemical composition of hydrothermal fluids and sulfides; new approaches are required to constrain subsurface processes in seafloor hydrothermal systems.

Sulfur isotope studies of seafloor hydrothermal vent systems have been particularly instructive for determining sulfur sources (i.e. sulfur from the leaching of igneous rocks and sulfur from the reduction of a small amount of admixed seawater-derived sulfate) and evolution of sulfide deposits (Shanks, 2001; Ono et al., 2007). Because subsurface hydrothermal processes greatly affect the distribution of base metals (such as Cu, Zn and Fe) and associated trace elements (such as Se, Mo, Sb and Ge), it is expected that the study of the variations of their natural isotopic abundance may also provide important constraints on seafloor hydrothermal systems. Various metals and metalloids have been investigated recently in seafloor hydrothermal systems at mid-oceanic ridges and ridge flanks and include Fe (Sharma et al., 2001; Beard et al., 2003b; Rouxel et al., 2003a; Rouxel et al., 2004b; Severmann et al., 2004), Cu (Zhu et al., 2000; Rouxel et al., 2004a), Zn (John et al., 2008), Se (Rouxel et al., 2004b), Mo (McManus et al., 2002), Sb (Rouxel et al., 2003b) and Tl (Rehkämper et al., 2004).

It has been demonstrated that the isotopic compositions of Fe in hydrothermal fluids differ significantly from the isotope composition of the source rock (Sharma et al., 2001; Beard et al., 2003b; Rouxel et al., 2004b; Severmann et al., 2004) and that hydrothermal systems may

impart a diagnostic isotopic signature to Fe released to the oceans from seafloor venting (Beard et al., 2003b; Chu et al., 2006; Severmann et al., 2004). However, despite these initial investigations, the factors influencing Fe isotopic variability in seafloor hydrothermal systems are poorly constrained. Specifically, we have little understanding of the isotope variations between vent types (black or white smokers) or reaction zone alteration processes. Fe isotope fractionation during sulfide precipitation also remains poorly constrained because Fe-isotope fractionation factors may be dependent on the kinetics of precipitation and pathways of sulfide formation (Butler et al., 2005) as well as equilibrium isotope effects, which are dependant on sulfide mineralogy and temperature of precipitation (Polyakov, 1997; Polyakov and Mineev, 2000; Polyakov et al., 2007).

In this study, we investigate Fe isotope systematics of hydrothermal fluids and sulfide precipitates from the hydrothermal fields at East Pacific Rise (EPR) 9-10ºN. The hydrothermal field at EPR 9-10ºN is located in a well-studied segment of the EPR between the Clipperton and Siqueiros Fracture Zones (e.g. Detrick et al., 1987; Haymon et al., 1991; Haymon et al., 1993; Fornari et al., 1998; Shank et al., 1998; Von Damm, 2000; Von Damm, 2004). The vent fluid chemistry in the area has been well documented and previous studies have reported temporal evolution chemical and isotopic properties of the vent systems in relation to magmatic events (Shanks et al., 1995; VonDamm et al., 1997; Shanks, 2001; Von Damm, 2004). Hence, hydrothermal vents at EPR 9-10ºN provide a unique opportunity to study coupled Fe- and S-isotope systematics in hydrothermal vents and sulfides over a range of temperature, fluid composition and hydrothermal stages. By investigating paired Fe-isotope compositions of hydrothermal fluids and sulfides from the same vent, we evaluate the importance of temperature and mineralogy on Fe isotope fractionation during sulfide precipitation at the seafloor. In addition, we discuss the potential fluid evolution in the upflow zone, such as subsurface sulfide precipitation in producing significant variability of Fe-isotope composition of hydrothermal fluids. Further constraints on Fe isotope fractionation processes are also investigated by exploring systematics between Fe-isotopes, S-isotopes and trace metal contents in hydrothermal sulfide minerals.

2. Geological Setting

The neovolcanic zone of the EPR between 9ºN and 10ºN is marked by a pronounced axial summit trough (AST), a ridge-parallel, elongate collapse feature that can be up to 15 m deep (Fornari and al, 1998). Most of the volcanic eruptions along the EPR are sourced in the AST, but off-axis eruptions are also known and during axial eruptions lava flows can extend several km on either side of the axis (Perfit et al., 1994; Schouten et al., 1999). Eighteen high temperature hydrothermal vent sites have been identified on the EPR between 9ºN and 10ºN (**Figure 1).** Hydrothermal activity has ranged from focused discharge of phase-separated high-temperature fluids (up to 403ºC) to low-temperature (<20ºC) diffuse venting (Von Damm and Lilley, 2004). The temporal evolution of vent systems in relation to magmatic events has been well documented (Von Damm et al., 1997; Von Damm, 2004). It has been shown that the hydrothermal vent fluids at 9º50´N have undergone unprecedented chemical changes from 1991–2002, probably related to phase separation and changes in the depth to the heat source driving the hydrothermal system at this site. These changes are manifest in variation of Cl and Na contents of the fluids by more than an order of magnitude during this time period, and by profound changes in the concentrations of other chemical species as well as temperature (Von Damm et al., 1997; Von Damm, 2004). Strontium isotope variations in vent fluids from 9º46´N-9º54´N have been also reported and were interpreted as evidence for a non-zero Mg fluid component that derived from low temperature seawater-basalt reactions (Ravizza et al., 2001).

Four hydrothermal vent sites (K-vent, Tica, Biovent and the Bio9 vents) sampled during the Atlantis/Alvin cruise AT11-20 in November 2004 were selected for this study. The high-temperature vents Bio9, Bio9' and Bio9'' (383ºC) and lower-temperature vent Tica (344ºC) are located at 9º50´N within an area sometimes referred to as the "Hole-to-Hell" (Shank et al., 1998) where the most dramatic changes in the hydrothermal systems have taken place. Prior to 1994, Bio9 was the only high temperature vent sampled while by 1994, the Bio9´ vent was a distinct individual black smoker. Bio9" is the third distinct smoker in the area and was initially sampled in 2002 (Von Damm, 2004). Hydrothermal fluids from Tica vent (344ºC) and Biovent (331ºC) were sampled from large beehive structures, surrounded by vent fauna (Shank et al., 1998; Le Bris et al., 2006) and characterized by shimmering water venting through the beehive. Because the beehives collapsed on contact with Alvin's arm, sulfide samples have not be recovered at both sites. The fluid samples were obtained from a clear venting orifice after beehive removal. K-vent at 9º29.8'N is the most southerly active vent sampled in this study (Von Damm, 2000). K-vent

has a distinctly lower temperature than other vents (203ºC), lower than the temperature previously reported by (Von Damm, 2000) in 1991 (263ºC).

3. Samples description

Three main types of hydrothermal deposits were recovered: (1) Cu-rich chimneys (black smokers) from Bio9''; (2) Zn- and Fe-rich chimneys and diffusers at K-vent; and (3) inactive massive sulfide deposits from the Bio9 area and an off-axis site. Reflected light microscopy was used for mineral identification and textural interpretations. Descriptions of hydrothermal deposit types and representative mineralogy are presented below. Hydrothermal fluids from four active vents (K-vent, Bio 9'', Tica and Biovent) were also recovered and are discussed separately in Section 4.

3.1. Cu-rich chimneys (black smokers)

Deposits characterized by abundant Cu-rich sulfide (i.e. chalcopyrite) and are typical of black smokers such as Bio 9'' that formed at temperatures higher than 300°C. The hydrothermal chimney recovered at Bio9'' has a wide trunk (~ 40 cm wide) that bifurcates into two orifices, one that was venting vigorously, and a second inactive one (**Fig. 2**). Sample ALV-4057-M1 represents the uppermost 40-50 cm of the black smoker, venting fluid at a temperature of 383ºC (fluid samples ALV-4057-W1&W2). The entire sample M1 has been divided into various pieces (#A1 to #A6 and #B1) that represent sections from bottom to top (**Fig. 3**). M1 is characterized by a well-zoned mineralogy across the chimney wall that varies in thickness from 1 to 4 cm. All samples are characterized by a thick inner layer of euhedral to massive chalcopyrite. Anhydrite is ubiquitously associated with chalcopyrite within the chimney wall but may also occur as cm-wide patches inside the open conduit. The presence of anhydrite reflects active incorporation of seawater and mixing with the high temperature hydrothermal fluid within the chimney interior (e.g. Tivey, 1995a). The external cm-wide wall is composed mainly of pyrite, marcasite and variable abundance of sphalerite.

3.2. Zn- and Fe-rich chimneys and diffusers

The deposits are typically characterized by varying proportion of pyrite, marcasite and sphalerite, which formed from hydrothermal vents emitting fluids at lower temperature and lower metal concentrations than black smokers. Most of the deposits are porous and may be composed of multiple conduits. The shapes range from diffusers (i.e. beehives) to typical chimneys.

185 *3.2.1. K-vent:* The deposit at K-vent is composed of a sulfide mound with numerous little spires
186 that emanate clear fluid (**Fig. 2**). The base is approximately 3 m wide and is heavily colonized by
187 *Alvinella,* sea anemones and vent crabs. Sample ALV-4053-M1 is from the upper part of a spiry
188 chimney. It is 73 cm long and was thickly colonized by *Alvinella.* The removal of the chimney
189 during sampling by Alvin caused vigorous venting of fluid from a small, marcasite-lined orifice
190 with a temperature at about 203ºC. The upper part of the chimney consists of a beehive colonized
191 by *Alvinella* and is composed of sphalerite, pyrite and marcasite and displays multiple tortuous
192 conduits lined with fine-grained sphalerite. Sample ALV-4053-M1 has been divided into 5
193 sections (#A1 to #A5) from the bottom to the top (**Fig. 3**). Samples #A1 and #A2 correspond to
194 the base of the chimney where the hydrothermal fluid was sampled (fluid samples ALV-4053-
195 W1&W2). The thin (5mm) chimney wall is composed of euhedral, bladed marcasite with minor
196 sphalerite, galena and chalcopyrite along joints. The exterior of the chimney wall is composed of
197 fine-grained pyrite with variable enrichment of marcasite, sphalerite and minor galena. Samples
198 A3 to A5 were recovered from the central part of the beehive structure and are composed of
199 euhedral sphalerite along the conduit walls with minor galena and variable enrichment of pyrite
200 and marcasite. Similar mineral assemblages, characterized by significant galena enrichment,
201 which is unusual for unsedimented MOR hydrothermal systems, have been reported previously at
202 K-vent chimney (Peng and Zhou, 2005).
203
204 *3.2.2. Zn-Fe-rich inactive deposits*:
205 Sample ALV-4053-M2 and ALV-4053-M3 are characterized by relicts of chimney
206 structures with a central conduit composed of euhedral, coarse-grained sphalerite coated with
207 soft, amorphous material (possibly silica mixed with Fe-oxyhydroxides) reflecting late-stage
208 mineralization leading to extinction of hydrothermal activity. Abundant galena and pyrite may
209 also occur in association with sphalerite. The external wall is composed of mixed assemblages of
210 fine-grained sphalerite, marcasite and silica. In some case, microcrystalline marcasite lined
211 ancient *Alvinella* tubes. Samples ALV-4053-M2 and ALV-4053-M3 have been recovered in the
212 vicinity of K-Vent and have similar mineralogy.
213 Sample ALV-4057-M2 (**Fig. 2**) is from an extinct sulfide structure just north of Bio9'' vent. Relicts of a central vent conduit are lined with euhedral bladed marcasite forming mm-thick
214 layers. The core of the chimney wall is characterized by fine grained sphalerite with only minor
215 marcasite. Euhedral to massive pyrite may also occur across the chimney wall. The external wall
216 is composed of fine-grained to acicular marcasite with small amounts of Fe-oxides. The
217

abundance of relict *Alvinella* tubes and the enrichment of Zn suggest also that this sample could be related to a Zn-rich diffuser vent-type.

Sample 4059-M3 is also an extinct chimney near the Bio9 area and is characterized by an central conduit lined with euhedral marcasite. Coarse-grained sphalerite associated with massive pyrite can be locally enriched across the chimney wall. Fine-grained to colloform pyrite with minor sphalerite may occur along fossil worm tubes.

Sample ALV-4059-M4 has been recovered from the top 1m of a 9-m tall inactive chimney off-axis (300m from AST). The interior of the former active vent is composed of sphalerite forming cm-wide layers, followed by fine grained assemblages of sphalerite and pyrite grading locally to more massive pyrite. Botryoidal sphalerite and pyrite form the external wall, which is coated by Fe-oxyhydroxides and amorphous silica.

3.3. Fe-rich massive sulfides.

Fe-rich massive sulfides have been recovered mainly from the Bio 9 area. In samples ALV-4058-M1 and ALV-4059-M2 (**Fig. 2**), pyrite is the major mineral occurring generally as anhedral to euhedral crystals. Relicts of worm tubes may be found and are completely mineralized by pyrite. The external crust of the sample is composed of Fe-oxide with minor silica. Different generations of sulfides and the lack of chimney structures reflect extensive remineralization of sulfides following hydrothermal diagenesis as described by Hannington et al. (1995). Field observations and petrographic evidence suggests that Fe-rich massive sulfides formed from late-stage mineralization of collapsed chimney fragments at the seafloor. The lack of sphalerite enrichment in the massive sulfides is also consistent with late-stage dissolution of any previously precipitated sphalerite, whereas the lack of chalcopyrite suggests mostly low-temperature (<250°C) fluid circulation.

4. Analytical Methods

4.1. Hydrothermal fluid sampling and chemical analysis

Eight hydrothermal fluids from four active vents were collected with Alvin using the 750 ml titanium major (Von Damm et al., 1985). Briefly, the Ti-samplers are filled using a titanium snorkel that can be inserted directly into the vent orifice. Immediately after the recovery, the pH was measured onboard and 30 mL sub-aliquots saved for the determination of $^{34}S/^{32}S$ isotope

ratios. Those fluid aliquots were extracted from the Ti-samplers using gas-tight syringes and transferred directly into evacuated glass bottles that contain a pre-weighed amount of Zn-acetate [$Zn(CH_3COO)_2 \times 2H_2O$] to precipitate ZnS. All samples for S-isotope analysis were prepared in duplicate and stored for later analysis at the USGS following the methods described in Shanks (2001). The remaining fluid solutions in the Ti-samples were then transferred to an acid cleaned bottle and acidified with ultrapure HCl (1mL per 500mL). Due to the high concentrations of metals in the hydrothermal solutions, precipitation often occurs within the titanium samplers as they cool to the ambient temperature. Those insoluble or precipitated particles remaining in the Ti-samplers are recovered for chemical analysis when the samplers are disassembled by rinsing with Milli-Q water and acetone and filtered through 0.45μm filters. This fraction is hereafter called "dregs"

Major cation concentrations (Na, K, Mg, Ca) were determined by ion-chromatography at WHOI and trace elements (Fe, Cu, Mn, Co, Zn, Cd) by high-resolution ICPMS *Element2*. Fe isotope ratios were determined at WHOI on a *Neptune* MC-ICPMS following the method described in Rouxel et al. (2005) and as described below. The fluid samples were stored acidified for about 6 months before analysis. In some case, particles remaining in the acidified bottles (presumably sulfides) were filtered through 0.2μm filters and the two fractions were analyzed. Both the DREGS and fluid particles were subsequently digested with distilled HNO_3 and HCl, evaporated and analyzed using the same procedure as for sulfide samples.

4.2. Hydrothermal sulfide sampling and chemical analysis

Hydrothermal sulfide deposits were collected with Alvin and split in various subsamples and stored dried in plastic containers. Samples were crushed on-shore between two plexiglas discs inside a Teflon bag using a hydraulic press. Sulfide grains were collected using 500 μm and 1.0 mm sieves and mono-mineral sulfide phases were isolated by hand-picking under binocular microscope. For each sample, mineral grains corresponding to a weight of 15 to 50 mg were picked in order to obtain a representative sulfide component. To assess possible sample heterogeneity, we also separated minerals with different crystal habits and these were individually analyzed.

Representative splits of mineral separates were used for S-isotope analysis at USGS following the procedure of Shanks (2001). Fe-isotope analysis and major and trace element determination were performed at WHOI on the same aliquots of the mineral separates for S-isotopes. Sulfides were weighted in 15 mL Teflon beakers and dissolved using 5 mL of

concentrated trace-metal grade HNO_3. After evaporation on a hot plate at 60°C, complete dissolution and Fe oxidation was achieved by a second evaporation step using 5mL of concentrated HCl and HNO_3 (1:2 volume). The dry residue was then dissolved in 5 mL of 6N HCl and trace H_2O_2 by heating at 40°C in a closed vessel. A fraction of the solution, corresponding to 100μg of Fe was then used for chemical separation for Fe-isotope analysis (see below) whereas another fraction, corresponding to 100μg of sulfide matrix was evaporated and diluted to 5 ppm with 2% HNO_3 (i.e. dilution factor of 200,000) for chemical analysis using high-resolution ICPMS.

Concentrations of ^{57}Fe, ^{65}Cu, ^{66}Zn, ^{44}Ca, ^{75}As, ^{82}Se, ^{208}Pb were determined by high-resolution ICPMS *Element2* operated at WHOI. Briefly, sample solutions, diluted with 2% HNO_3 were analyzed using the high-resolution mode of the ICPMS which permits separation of isotopes from isobaric interferences, such as $^{40}Ar^{16}O^{1}H$ on ^{57}Fe and $^{40}Ar^{35}Cl$ on ^{75}As. Solutions were introduced into the plasma using a quartz spray chamber system equipped with a microconcentric PFA nebulizer operating at a flow rate of about 100 μL/min. For each element, ICPMS sensitivity was calibrated using matrix matched standard solutions corresponding to synthetic sulfide matrices. We verified that this standardization is valid for chalcopyrite and sphalerite measurements by analyzing standard solutions with molar ratios of Cu/Fe and Zn/Fe =1.

4.3. Fe-isotope composition

Fe isotope compositions were determined with a Finnigan *Neptune* multicollector inductively coupled plasma mass spectrometry (MC-ICPMS) at WHOI using the method described previously (Rouxel et al., 2003a; Rouxel et al., 2005; Rouxel et al., 2007). The *Neptune* instrument permits high precision measurement of Fe isotope ratios without argon interferences using the high-mass resolution mode (Malinovski et al., 2003; Weyer and Schwieters, 2003; Arnold et al., 2004; Poitrasson and Freydier, 2005). Mass resolution power of about 8000 (medium resolution mode) was used to resolve isobaric interferences, such as ArO on ^{56}Fe, ArOH on ^{57}Fe, and ArN on ^{54}Fe. Instrumental mass bias is corrected using Ni isotopes as internal standards. The method, which has proved to be reliable for the Neptune instrument, involves deriving the instrumental mass bias by simultaneously measuring the Ni standard solution. We also used the "sample-standard bracketing" technique to correct for instrumental mass discrimination by normalizing Fe isotope ratios to the average measured composition of the standard that was run before and after the sample. Fe isotope compositions are reported relative the Fe-isotope standard IRMM-14 using the following standard delta notation:

$$\delta^{56}Fe=1000 * [(^{56}Fe/^{54}Fe)_{sample}/(^{56}Fe/^{54}Fe)_{IRMM\text{-}14} -1] \quad (1)$$

Sample purification for mass spectrometry analysis was undertaken by anion-exchange chromatography in a clean room environment following previously defined protocols (Beard et al., 2003a; Rouxel et al., 2003a; Rouxel et al., 2005). For hydrothermal fluids, not more than 15mL of water were dried down in PTFE beakers with 1mL of concentrated HNO_3. The dry residue was then dissolved with 4mL 6N HCl and a trace of H_2O_2. Purified samples were diluted to 1.5 ppm of Fe and Ni and introduced into the plasma using a double quartz spray chamber system (cyclonic and double pass) and a microconcentric PFA nebulizer operating at a flow rate of about 100 μL/min. Precision of Fe-isotope analyses in water samples was evaluated using a seawater-like matrix doped with the Fe standard. We obtained a $\delta^{56}Fe$ precision of 0.10‰ (2σ, n=10) for Fe concentrations as low as 5μM.

Based on > 50 replicate dissolutions, purifications and analyses of the BHVO-1 standard (Hawaiian basalt), we obtained a $\delta^{56}Fe$ average of 0.10 with a precision of 0.09‰ (2σ). The relationships between $\delta^{56}Fe$ and $\delta^{57}Fe$ of the samples analyzed in this work plot on a single mass fractionation line and only $\delta^{56}Fe$ values are discussed in this paper.

5. Results

5.1. Hydrothermal fluid elemental composition:

The hydrothermal fluids collected from the four vent sites (**Table 1**) display a significant range of temperatures (203 to 383°C), salinity (Na concentration between 300 to 500 mM), and Fe concentrations (100 to 3400 μM). The low-Mg contents (<5 mM) for most of the high-temperature hydrothermal fluids reflect minimal dilution with seawater (Mg = 53 mM). In some cases, hydrothermal fluids with Mg contents up to 25 mM (e.g. Biovent, **Table 1**) were obtained suggesting significant entrainment of seawater during sampling. **Table 2** reports the calculated end-member hydrothermal fluid compositions for all elements measured. The calculation of end-member fluid composition also includes the correction for the dregs, which are fine precipitates assumed to have formed by precipitation from hydrothermal fluid after collection in the Ti-sampler. Because of the uncertainty in the dregs recovery and the possibility that small pieces of the sulfide chimney were also entrained during sample collection, we verified that the dregs represent a minor fraction of the total dissolved Fe concentration. For all samples, the dissolved

353 fraction is >90% of the total Fe for the sample. However, the importance of the dregs is more
354 pronounced for Cu and Co concentrations and, to a lesser extent, for Pb, Zn and Cd.
355 As none of the end-member vent fluids have Na concentrations equal to that of seawater
356 (**Table 2)**, it is likely that they have all undergone phase separation. Fluids from Biovent, Bio9"
357 and Tica have lower Na concentration than seawater and likely correspond to the vapor phase
358 resulting from sub-critical phase separation. In contrast, higher Na concentration (together with
359 higher chlorinity) at K-vent has been previously reported by Von Damm (2000), suggesting that
360 the fluid represents a brine phase. K-vent fluid has lower Fe concentration, which is likely due to
361 the lower temperature of the vent and subsurface sulfide precipitation. As expected, Cu and Co
362 concentrations in all end-member fluids at EPR 9-10°N display a sharp decrease with temperature
363 below 350°C, which is consistent with previous studies (Metz and Trefry, 2000). Cd and Zn
364 concentrations show also some temperature dependence while Pb lacks any depletion in lower-
365 temperature vents such as K-vent. The unusual Pb enrichment at K-vent (i.e. relative to other
366 trace metals) is also reflected in the chimney mineralogy with the abundant occurrence of galena
367 associated with sphalerite and marcasite. Biovent is unlike any other vents as it contains low Fe
368 concentration (~290 μM) despite measured vent temperatures of up to 331°C.
369
370 *2.2. Hydrothermal sulfides elemental composition:*
371
372 In order to determine quantitatively the purity of mineral separates of hydrothermal chimney
373 and massive sulfides, we determined the modal mineralogy of mineral separates (supplementary
374 materials) based on their bulk chemical composition reported in **Table 3**. Results show that
375 chalcopyrite and pyrite separates represent generally pure phases (>90 mol%). However, mineral
376 inclusions in sphalerite could not be avoided, and, consequently, contain variable proportion of
377 pyrite, galena and chalcopyrite. For example, the Zn-rich active chimney from K-vent is
378 characterized by strong Pb enrichments (up to 16 wt%) reflecting common occurrence of galena
379 that was precipitated within the chimney wall together with sphalerite. In contrast, inactive Zn-
380 rich chimneys have relatively lower Pb concentrations (< 0.7 wt%).
381 Other elements such as As and Se in hydrothermal sulfides are present only as trace amounts
382 and vary greatly between minerals (e.g. sphalerite, pyrite, chalcopyrite) and distinct geochemical
383 signatures are recorded between vent deposits (**Table 3)**. It has been generally observed that As is
384 preferentially enriched in low-temperature vent fluids (Metz and Trefry, 2000) and Zn-rich
385 sulfide deposits (Fouquet et al., 1988; Hannington et al., 1995; Tivey et al., 1999) and our results
386 at EPR 9-10°N are generally consistent with the previous studies. As has been observed to be

387 associated with sphalerite in the form of accessory minerals such as Cu-sulfosalts like tennantite-
388 tetrahedrite, but these minerals were not observed in our samples. It is likely that As is held in
389 pyrite, marcasite, sphalerite and galena as trace element substitutions or inclusions (Hannington et
390 al., 1995; Fouquet et al., 1996; Tivey et al., 1999). In this case, various As enrichments are
391 expected depending on physicochemical conditions of sulfide deposition in the chimney structure.
392 We note, however, that we did not find systematic relationships between As or other trace
393 elements and Fe- and S-isotope composition. Bio 9'' yields the highest value of selenium which
394 is consistent with previous studies showing strong enrichment of Se in high temperature
395 hydrothermal sulfides (Auclair et al., 1987; Rouxel et al., 2004b). The comparison of Se
396 concentration between marcasite/pyrite (from 2 to 90ppm) and chalcopyrite (from 1,200 to 1,600
397 ppm) at Bio 9" also confirms that Se partition preferentially into chalcopyrite relative to pyrite
398 (Yamamoto et al., 1983; Rouxel et al., 2004b) and suggest minor chalcopyrite inclusions in pyrite
399 mineral separates.
400
401 *5.3. S-isotope composition*
402
403 The $\delta^{34}S$ values of hydrothermal fluids at EPR 9-10ºN range from 3.1 to 5.4‰ and $\delta^{34}S$
404 values do not correlate with vent temperature or end-member fluid composition. The overall
405 range of $\delta^{34}S$ values (2.3‰) is consistent with previous reports of S-isotope composition of vent-
406 H_2S collected at EPR 9-10ºN between 1990-1995 (Shanks, 2001). Although Tica, Biovent and
407 Bio9'' vents are from the same area at 9º50'N, S-isotope composition of H_2S range from 3.1‰ to
408 5.4‰ indicating local heterogeneity.
409 The $\delta^{34}S$ values of sulfides from the chimney wall of Bio 9'' display a range of 2.4‰ (**Table**
410 **3**). Pyrite and marcasite have $\delta^{34}S$ values ranging from 1.2 to 2.0‰ whereas chalcopyrite and
411 sphalerite yield systematically higher $\delta^{34}S$ values between 2.2 to 2.6‰. Vent H_2S at Bio 9" yields
412 $\delta^{34}S$ values of 3.1 and 3.2‰, which correspond to an enrichment of ^{34}S by up to 0.9‰ relative to
413 chalcopyrite lining the interior of the chimney (**Fig. 6**). Similar features are also observed at K-
414 vent, where euhedral marcasite in the interior of the chimney yields lower $\delta^{34}S$ values by up to
415 1.7‰ relative to vent H_2S.
416 Sulfide $\delta^{34}S$ values at K-vent (pyrite, marcasite, sphalerite +/- galena) display a range of 2‰
417 and define two distinct groups. One group of sulfides with $\delta^{34}S$ values of ~ 2‰ are characterized
418 by low Zn-concentrations (<2 wt%) and correspond to pyrite-marcasite mineral assemblages
419 precipitated near the interior of the chimney wall (**Table 3**). The other group of sulfides with $\delta^{34}S$

values around 3.3‰ is characterized by higher Zn-concentrations and correspond to pyrite-sphalerite-galena assemblages that precipitate either within the chimney wall or along diffuse conduits.

$\delta^{34}S$ values of pyrite from inactive deposits range from 0.7‰ to 3.8 ‰ and overlap with most $\delta^{34}S$ values obtained for active chimneys at unsedimented ridges (Shanks, 2001; Rouxel et al., 2004b). Interestingly, $\delta^{34}S$ values of pyrite from Fe-rich massive sulfides are higher than $\delta^{34}S$ values of pyrite-marcasite from inactive Zn-Fe-rich chimneys (**Table 3)**. In general, sphalerite-rich samples from inactive Zn-rich chimneys display higher $\delta^{34}S$ values than pyrite-marcasite in the same sample.

5.4. Fe-isotopes composition

The $\delta^{56}Fe$ values of end-member hydrothermal fluids at EPR 9-10°N vary between –0.25 and –0.67‰ **(Table 2),** which is similar to the range of $\delta^{56}Fe$ values reported by Beard et al. (2003b) from the same area. The largest $\delta^{56}Fe$ variations are found for low-Fe fluids, such as those found at K-vent and Biovent. K-vent yields the highest $\delta^{56}Fe$ at around –0.25‰ whereas Biovent yields the lowest $\delta^{56}Fe$ values down to –0.69‰. Fe-isotope compositions of dissolved Fe in hydrothermal fluid at Bio 9'' vary between –0.38 to –0.43‰ whereas vent fluid particles (dregs) have lower $\delta^{56}Fe$ values by about 0.1‰ (**Table 1**). Lower $\delta^{56}Fe$ values (between –0.33 to –0.72‰) for the dregs are observed at Biovent and K-vent while the lowest $\delta^{56}Fe$ values for the dregs (down to –1.8‰) are reported for Tica vent. Similar Fe-isotope fractionation between dissolve Fe and insoluble particles has been previously reported by Beard et al. (2003b) at EPR 9-10°N. In particular, $\delta^{56}Fe$ values as low as –1.6‰ for fluid particles were found at Bio9 vent that was sampled in 1994. However, these low $\delta^{56}Fe$ values were not reproduced during subsequent sampling of the same hydrothermal vent one year after (Beard et al., 2003b).

Chalcopyrite at Bio9'' displays a limited range of $\delta^{56}Fe$ values between –0.11 to –0.33‰ which is, on average, slightly higher by 0.14±0.09‰ relative to the composition of associated vent fluids. The relationship between $\delta^{56}Fe$ values in vent fluids and chalcopyrite at Lucky Strike, Rainbow and Logatchev hydrothermal fields also suggests small, but positive Fe-isotope fractionation during chalcopyrite precipitation (**Fig. 4**). It is important to note, however, that $\delta^{56}Fe$ values of chalcopyrite and vent fluids reported for other seafloor hydrothermal vent fields are not necessarily from the same vent, precluding a direct comparison of Fe-isotope fractionation factors with our study.

As previously seen by Rouxel et al. (2004b) at the Lucky Strike hydrothermal field, $\delta^{56}Fe$ values of pyrite and marcasite tend to be systematically negative compared to coexisting chalcopyrite. Based on 6 chalcopyrite-marcasite pairs at Bio9'', we calculated an apparent Fe-isotope fractionation of 0.94±0.13‰ between chalcopyrite and marcasite. Relatively smaller differences in $\delta^{56}Fe$ values between vent fluids Fe^{2+} and marcasite along the chimney wall were found at K-vent and yielded an average Fe-isotope fractionation between Fe^{2+}_{aq} and FeS_2 of 0.52±0.12‰. These results suggest a systematic relationship between mineralogy and Fe-isotope composition in hydrothermal sulfides as discussed below.

6. Discussion

6.1. Parameters affecting Fe-isotope composition in hydrothermal fluids:

The $\delta^{56}Fe$ values for hydrothermal fluids and sulfides at EPR 9-10°N and other sites are summarized in **Figure 4**. Fe-isotope results at EPR 9-10° confirm that Fe-isotope composition of hydrothermal fluids and sulfides have negative $\delta^{56}Fe$ values relative to the bulk silicate Earth determined at 0.09‰ (Sharma et al., 2001; Beard et al., 2003b; Severmann et al., 2004; Dauphas and Rouxel, 2006). The variations of Fe-isotope composition of hydrothermal fluids, however, are significant and $\delta^{56}Fe$ values as low as -0.67‰ and as high as -0.09‰ have been observed in hydrothermal vent fluids along the Mid-Atlantic Ridge and East Pacific Rise. The potential processes controlling the Fe-isotope variability in hydrothermal fluids, including phase separation, high-temperature basalt alteration, and subsurface processes are discussed below.

Although phase separation is one of the fundamental processes controlling mid-ocean ridge vent fluid chemistry (e.g. Von Damm, 1995), several lines of evidences suggest only limited Fe-isotope fractionation during this process. First, Beard et al. (2003b) measured Fe-isotope composition of both the vapor and brine phases from the Brandon Vent at EPR 21.5°S and found not more than 0.15‰ difference between these two fluids. Secondly, although not spatially related, Fe-isotope compositions of the high salinity fluid at K-vent (i.e. Na above seawater) does not differ significantly from lower salinity, vapor-rich fluids at Tica vent (**Fig. 5**).

Using samples from Ocean Drilling Program (ODP) Site 801 in the Jurassic Pacific Oceanic crust, Rouxel et al. (2003a) observed significant Fe-isotope fractionation in secondary Fe-bearing minerals formed during low-temperature alteration. In particular, highly altered basalts that are depleted in Fe by up to 80% from their original Fe concentration displayed an increase in $\delta^{56}Fe$ values relative to fresh values (up to 1.3 ‰), which suggests preferential

leaching of light Fe isotopes (between –0.5‰ and –1.3‰) during alteration. Similar processes also may occur during high-temperature alteration of basalt, for example, through the formation of secondary minerals (e.g. Mg-Fe amphibole) in the high-temperature reaction zone. Although Fe-isotope compositions in end-member hydrothermal fluids are generally consistent with an enrichment of light Fe isotopes during basalt alteration, it is unclear if such process may explain the range of δ^{56}Fe values between -0.25 to –0.67‰ found in the hydrothermal fluids at EPR 9-10°N.

As suggested by Rouxel et al. (2004b), significant Fe-isotope fractionation in hydrothermal fluids may also occur during Fe-sulfide precipitation in subsurface environments. In order to test further this hypothesis, we compared δ^{56}Fe values with Fe/Mn ratios of vent fluids at EPR 9-10°N (**Fig. 5**). While Fe is readily depleted in hydrothermal fluids due to subsurface sulfide precipitation, Mn tends to behave conservatively. Accordingly, Fe/Mn ratios are a good indicator of subsurface metal sulfide precipitation (Seewald and Seyfried, 1990). The lack of correlation between Fe/Mn ratios and Fe-isotope compositions argues against significant isotope effect during subsurface sulfide precipitation which contrasts with previous studies (Rouxel et al., 2004b; Sharma et al., 2001). The discrepancy between the apparent lack of Fe-isotope fractionation during Fe-loss in subsurface environments and the large Fe-isotope fractionation observed between vent fluid and sulfides (**Fig. 6**) can be reconciled by considering the potential effects of kinetic vs. equilibrium isotope fractionation and pathways of sulfide formation as presented in section 6.2.

Previously reported Sr isotope compositions in vent fluids from the EPR 9°50'N area have shown the existence of a non-zero Mg fluid component that derived from low temperature seawater-basalt reactions (Ravizza et al., 2001). In particular, this low-temperature fluid component may account for up to 10% by volume of the Biovent fluid. Since Biovent yields the lowest δ^{56}Fe values down to –0.69‰, it can be suggested that this additional fluid component may be characterized by very low δ^{56}Fe values. Similarly, the circulation of isotopically fractionated low-temperature fluids (down to -2.0‰) on ridge-flanks have been suggested previously (Rouxel et al., 2003a) to explain strongly negative δ^{56}Fe values of Si-Fe-rich hydrothermal deposits in the oceanic crust at ODP Site 801C. All together, these results suggest that Fe-isotopes in hydrothermal fluids are mostly controlled by fluid mixing processes in the upflow zone rather than high-temperature reaction zone processes.

6.2. Potential effects of kinetic vs. equilibrium Fe-isotope fractionation:

Using the reduced isotopic partition function ratios of FeS_2 and Fe(II)-aquo-chloro complexes determined previously (Polyakov, 1997; Polyakov and Mineev, 2000; Schauble et al., 2001; Polyakov et al., 2007), it is possible to estimate the isotope fractionation factors α between FeS_2 and $FeCl_4^{2-}$ or $Fe(H_2O)_6^{2+}$ to be ~1.0015 at 350°C and ~1.002 at 250°C. However, this positive fractionation factor is opposite to the isotope fractionation between pyrite-marcasite and vent fluids obtained in this study (**Fig. 6**). In addition, Butler et al. (2005) investigated Fe isotope fractionation during FeS (i.e. mackinawite) precipitation from $Fe(II)_{aq}$ solutions and demonstrated that the zero-age precipitates have systematically negative $\delta^{56}Fe$ values relative to the fluid, by approximately –0.8‰. During aging, the precipitates and the fluid tend to converge towards the same isotopic composition. The minimum difference that is observed after 170 hours is –0.3 ‰, but this may still not represent the isotope fractionation at equilibrium. The negative $\delta^{56}Fe$ values of the precipitate relative to the fluid is interpreted to reflect a kinetic isotope effect associated with ligand exchange between hexaqua Fe(II) and aqueous sulfide complexes (Butler et al., 2005). Although these experiments were performed at temperatures less than 40°C, they may provide important constraints on Fe-isotope fractionation in hydrothermal pyrite. For example, in the case of relatively slow precipitation of pyrite in subsurface environments due to conductive cooling of the fluids, limited Fe-isotope fractionation is expected. In contrast, when rapid precipitation of pyrite occurs as a result of mixing with seawater, typical of chimney environments, significant kinetic Fe-isotope fractionation might be expected.

Our Fe-isotope results showing Fe-isotope fractionation factors between vent fluid and pyrite/marcasite determined at 0.58±0.13‰ and 0.77±0.07‰ for K-vent and Bio9" respectively are consistent with kinetic isotope fractionation effects (**Fig. 6**). These results are also consistent with variable kinetic Fe-isotope fractionation effects (between 0.03 to up to 1.5‰) during rapid precipitation of the dregs (presumably FeS, Luther III et al., 2001) inside the Ti-bottle after fluid sampling (**Fig. 5**). In contrast, the precipitation of chalcopyrite along the chimney wall at Bio9" produces slightly positive Fe-isotope fractionation factors (0.14±0.09‰, **Fig. 6**). The lack of enrichment of light Fe-isotopes in chalcopyrite could result from attainment of isotope equilibrium for higher temperatures of precipitation together with smaller kinetic fractionation factors as discussed below.

6.3. S-isotope systematics and the origin of S-isotope disequilibrium in seafloor hydrothermal sulfides;

Sulfur isotope studies provide valuable information for determining sulfur sources and precipitation mechanisms in submarine hydrothermal deposits. Different mechanisms have been proposed to explain variations in the $\delta^{34}S$ values of sulfides in seafloor hydrothermal systems (e.g. Janecky and Shanks, 1988; Shanks, 2001) and indicate that sulfur has two major sources: (1) sulfur from the leaching of igneous rocks; (2) sulfur from the reduction of a small amount of admixed seawater-derived sulfate. Experimental and theoretical approaches provide models for the behavior of sulfur in seafloor hydrothermal systems (Janecky and Shanks, 1988) and suggest that H_2S in the reaction zone has an isotopic value of 1 to 1.5‰. The limited supply of sulfate through the 150°C anhydrite precipitation front into the high temperature reaction zone can account for the $\delta^{34}S$ variations of ~1.5 to ~4.5‰ and a further increase in $\delta^{34}S$ could result from sulfate reduction involving fresh basalt in the upflow zone where additional sulfate is added by seawater mixing or anhydrite dissolution. At EPR 9-10°N, $\delta^{34}S$ values of H_2S between 3.1 to 5.5‰ are generally consistent with previous models and suggest significant reduction of seawater sulfate (up to 20%); this result is confirmed by recent studies that add ^{33}S constraints to previous sulfur isotope approaches (Ono et al., 2007). The overall $\delta^{34}S$ variability of up to 2.4‰ between Tica, Biovent and Bio9'' vents from the same area at 9º50'N suggests also local heterogeneity of reduction of seawater sulfate in the reaction zone or upflow zone. Temporal variations of $\delta^{34}S$ values in hydrothermal vents in the 9º50'N area have also been reported (Shanks, 2001) and attributed to changes of seawater sulfate reduction during magmatic events.

As shown in **Figure 6**, consistent differences in $\delta^{34}S$ values are observed between sulfide pairs (chalcopyrite/pyrite or sphalerite/marcasite) as well as sulfide/H_2S pairs for two different chimneys (i.e. Bio 9" and K-Vent) formed at different temperature (383 and 203°C respectively). Based on the difference of $\delta^{34}S$ values between *coexisting* chalcopyrite and pyrite from individual samples at Bio 9", we calculate an isotope fractionation of 0.83 +/- 0.3‰ for chalcopyrite-pyrite pairs. This fractionation is opposite to the isotope *equilibrium* fractionation factor between pyrite and chalcopyrite at 360°C ($\Delta^{34}S_{\text{chalcopyrite-pyrite}} \sim -1.1‰$ Ohmoto and Goldhaber, 1997). Similar features were previously reported at other hydrothermal fields in many studies (Kerridge et al., 1983; Shanks and Seyfried, 1987; Bluth and Ohmoto, 1988; Woodruff and Shanks, 1988; Rouxel et al., 2004b). In general, lower $\delta^{34}S$ values for pyrite relative to vent H_2S, sphalerite, and chalcopyrite are interpreted as reflecting S-isotope disequilibrium during sulfide precipitation or

583 temporal variations such that present day $\delta^{34}S$ of H_2S does not correlate to inner wall sulfide
584 minerals at the scale we are able to sample (Shanks et al., 1998).
585 In a recent study, Ono et al. (2007) used multiple isotope systematics (^{32}S,^{33}S,^{34}S) to
586 discriminate between S-isotope processes in seafloor hydrothermal systems. It is shown that
587 pyrite/marcasite and chalcopyrite at Lucky Strike hydrothermal field are found to be in isotopic
588 disequilibrium, not only in $\delta^{34}S$, but also in $\Delta^{33}S$. Relatively higher $\Delta^{33}S$ and lower $\delta^{34}S$ values for
589 pyrite and marcasite compared to those of chalcopyrite were interpreted as the result of near-
590 equilibrium isotope exchange between seawater sulfate and vent H_2S during mixing in surface or
591 subsurface environments (Ono et al., 2007). We consider that similar isotope effects between
592 seawater sulfate and hydrothermal H_2S may explain lower $\delta^{34}S$ values for pyrite and marcasite at
593 K-vent and Bio 9'' relative to H_2S and chalcopyrite. At K-vent, the sulfide mound structure
594 allows significant seawater sulfate to be entrained and mixed with the hydrothermal fluid which
595 may promote S-isotope exchange with seawater during marcasite precipitation. At Bio9'',
596 marcasite is mainly precipitated in the external rim of the chimney wall and is isolated from the
597 high-temperature fluid by a cm-thick massive chalcopyrite lining. In this case, a strong gradient
598 between the hydrothermal fluid and seawater develops and permits local isotope exchange
599 between vent fluid H_2S and seawater SO_4^{2-}.
600
601 *6.4. Coupled Fe and S-isotope composition in sulfides: potential importance of sulfide*
602 *precipitation pathways*
603
604 As presented in **Figure 6,** pyrite/marcasite assemblages at K-vent show strong isotopic
605 disequilibrium *in both* Fe-isotopes and S-isotopes relative to the hydrothermal fluid. Pyrite and
606 marcasite at Bio9" vent have also distinctly lower $\delta^{34}S$ and $\delta^{56}Fe$ values relative to coexisting
607 chalcopyrite. Negative Fe-isotope values in pyrite likely results from kinetic isotope effects
608 during rapid sulfide precipitation in the chimney structure. In addition, pyrite-marcasite from
609 inactive chimneys and massive sulfides display a generally positive correlation between $\delta^{34}S$ and
610 $\delta^{56}Fe$ values (**Fig. 7**). These results suggest a control of formation mechanisms of pyrite (or
611 marcasite) and chalcopyrite on both Fe and S-isotope composition.
612 Several precipitation pathways of pyrite formation in hydrothermal systems have been
613 suggested (Schoonen and Barnes, 1991; Wilkin and Barnes, 1996; Rickard, 1997) and include the
614 formation of pyrite from FeS precursors by reaction with thiosulfate or polysulfide compounds
615 (Schoonen and Barnes, 1991) or with H_2S (Rickard, 1997). According to Ono et al. (2007), pyrite
616 formation via thiosulfate intermediates may promote isotope exchange between H_2S and seawater

617 SO_4^{2-} through the formation of thiosulfate and explain the isotope disequilibrium for pyrite and
618 marcasite (i.e. lower $\delta^{34}S$ values) relative to chalcopyrite. It is however unclear if similar
619 pathways may also produce lower $\delta^{56}Fe$ values. As suggested by Butler et al. (2005), $\delta^{56}Fe$ values
620 in pyrite (or its precursor) may be kinetically controlled by the rate of precipitation. Likewise,
621 negative $\delta^{56}Fe$ values in pyrite may be explained by a kinetic isotope effect during the
622 precipitation of FeS followed by the quantitative conversion of FeS to pyrite with minimal
623 isotope fractionation. When pyrite formation is rapid, such as during mixing between
624 hydrothermal fluid and seawater, the incorporation of Fe from FeS_{aq} into pyrite may be
625 sufficiently rapid to allow maximum kinetic isotope fractionation to be recorded in pyrite. In this
626 case, pyrite precipitated in chimney environments will be characterized by lower $\delta^{56}Fe$, due to
627 strong kinetic effects and lower $\delta^{34}S$ values, due to formation via thiosulfate intermediates (**Fig.**
628 **6**).

629 During precipitation of chalcopyrite from FeS precursors via reaction with H_2S (Cowper and
630 Rickard, 1989), it is expected that $\delta^{34}S$ values will be close to $\delta^{34}S$ values of vent H_2S (or near
631 isotope equilibrium values). S-isotope compositions of chalcopyrite at Bio 9" EPR 9-10°N are
632 generally consistent with this model (**Fig. 6**). Because chalcopyrite is expected to precipitate at
633 high-temperature (above 350°C), the lack of negative Fe-isotope fractionation associated with
634 chalcopyrite precipitation may result from the rapid establishment of isotope equilibrium between
635 FeS precursor, Fe(II)aq reservoir and $CuFeS_2$. In this case, the equilibrium Fe-isotope
636 fractionation factor $\Delta^{56}Fe$ between $CuFeS_2$ and Fe(II)aq (or FeS) is expected to be positive, as
637 already theoretically determined for pyrite and nickel sulfides (Polyakov and Mineev, 2000;
638 Polyakov et al., 2007). This issue needs to be further addressed through experimental
639 investigations at hydrothermal temperature. Similar equilibrium Fe-isotope fractionation between
640 FeS precursor and FeS_2 is also expected during slow formation of pyrite through the H_2S pathway
641 when the hydrothermal fluid is isolated from seawater. Such conditions may be found during
642 massive sulfide formation where several stages of remineralization at or below the seafloor (e.g
643 Hannington et al. 1995) may result in an increase of Fe- and S-isotope exchange (i.e. near
644 equilibrium fractionation) between vent fluids (or FeS precursor) and FeS_2. Higher $\delta^{34}S$ and $\delta^{56}Fe$
645 values of pyrite in massive sulfides, which are close to the average vent fluid values at EPR 9-
646 10°N (**Fig. 7**), are consistent with this model.
647
648 *6.5. Model of Fe and S isotope fractionation in seafloor hydrothermal systems:*
649

A schematic hydrothermal sulfide mound with different fluid flow paths is presented in **Figure 8**. A typical chimney complex may include a stockwork zone beneath the mound, emission of both high-temperature (350°C) and lower-temperature (100-250°C) fluids from the top of the mound together with diffuse flow (<100°C). Sulfide precipitation at the seafloor or in subsurface environments is either due to conductive cooling of the hydrothermal fluid and/or mixing of the hydrothermal fluid with ambient seawater. The effects of different fluid evolution on δ^{56}Fe composition of fluids and sulfides is illustrated in **Figure 8** and described as follows: (1) Direct venting of the end-member hydrothermal fluid and mixing with seawater at the seafloor will form mineralogically zoned chimneys with δ^{56}Fe and δ^{34}S values of chalcopyrite, sphalerite and pyrite/marcasite affected by various degrees of Fe-isotope kinetic fractionation and S-isotope exchange between seawater and H_2S. Variability of δ^{56}Fe values of the hydrothermal fluid through reservoir effects (i.e. Rayleigh fractionation) across the chimney wall is unlikely because quantitative models of fluid transport and chemical reaction demonstrate transport-dominated environments within black smokers (Tivey, 1995a; Tivey, 1995b) (2) Conductive cooling of the hydrothermal fluid in subsurface environments or formation of massive sulfides through multiple remineralization stages will produce pyrite with δ^{34}S and δ^{56}Fe values near isotopic equilibrium with the fluids (3) Lower-temperature chimneys (e.g. white to gray smokers) are expected to exhibit essentially the same δ^{34}S and δ^{56}Fe values as black smokers. This hypothesis, however, does not rule out the possibility of Fe-isotope variability in hydrothermal fluids due to rapid subsurface sulfide precipitation during seawater incorporation at the base of the chimney. (4) Fe-isotope systematics in warm diffuse flow are presently unknown, but may be characterized by very low δ^{56}Fe values. It is likely that biological activity could play a major role in lower temperature environment affect Fe and S concentrations (e.g. microbial H_2S and Fe(II) oxidation) and isotope compositions. It is also possible that such warm diffuse fluids, composed of admixed seawater partially reacted with basalt, could be subsequently entrained in high-temperature vent fluids and contribute to lower δ^{56}Fe values of the fluid emanating from black smokers.

7. Conclusion

In this study, we present coupled Fe and S isotope systematics for hydrothermal fluids and sulfides at EPR 9-10ºN to provide further constraints of the effects of the mineralogy and temperature of hydrothermal precipitates on Fe isotope signatures. The results show systematically lower δ^{56}Fe and δ^{34}S values in marcasite/pyrite relative to chalcopyrite and

683 hydrothermal fluids within a single chimney and suggest isotope disequilibrium in both Fe- and
684 S-isotopes. The concomitant Fe and S-isotope fractionation during pyrite/marcasite precipitation
685 is explained by (1) isotopic S-exchange between fluid H_2S and SO_4^{2-} during precipitation of pyrite
686 from FeS precursors by reaction with thiosulfate and (2) rapid formation of pyrite from FeS, thus
687 preserving negative Fe-isotope fractionation factors during FeS precipitation. In contrast, $\delta^{56}Fe$
688 and $\delta^{34}S$ values of pyrite precipitated in massive sulfides, either in the subsurface during
689 conductive cooling of the fluid (i.e. slow rate of precipitation) or during multiple stages of
690 remineralization, are expected to be similar to $\delta^{56}Fe$ and $\delta^{34}S$ values of the hydrothermal fluid.
691 This hypothesis is consistent with the limited range of $\delta^{56}Fe$ values between high-temperature,
692 Fe-rich black smokers and lower temperature, Fe-poor vents suggesting minimal Fe-isotope
693 fractionation during subsurface sulfide precipitation. It is also consistent with previous work
694 showing opposite Fe-isotope fractionation factors during kinetic Fe-sulfide (mackinawite)
695 precipitation (Butler et al., 2005) and equilibrium pyrite precipitation (Polyakov, 1997; Polyakov
696 and Mineev, 2000; Polyakov et al., 2007).

697 This study confirms initial investigations of Fe-isotope compositions in hydrothermal fluids
698 (Sharma et al., 2001; Beard et al., 2003b; Severmann et al., 2006) and suggests that seafloor
699 hydrothermal fluids define a range in Fe isotopic composition that is shifted to low $\delta^{56}Fe$ values
700 by -0.2 to -0.7‰ compared to igneous rocks. These results also suggest that $\delta^{56}Fe$ composition of
701 vent fluids may depend of numerous parameters such as rock alteration processes, pathways of
702 Fe-sulfide precipitation in subsurface environments and possibly phase separation processes. In
703 particular, considering the major importance of sulfide precipitation in the fractionation of Fe-
704 isotopes, the cooling and mixing history of the fluids and the effects of Fe/H_2S ratios in the vent
705 fluids and overlying hydrothermal plumes (Severmann et al., 2004) need further investigations.
706 The nature of volcanic rocks (basalt, felsic or ultrabasic rocks) and geological settings (tectonic
707 vs. magmatic dominated systems) remains also poorly constrained. One way to approach these
708 questions in the future would be to undertake time-series measurement of Fe-isotopes in
709 hydrothermal fluids following previous work on fluid chemistry (e.g. Von Damm and Lilley,
710 2004) and measure Fe-isotope composition in seafloor hydrothermal systems from various
711 settings, including back-arc hydrothermal systems and volcanic seamounts as well as diffuse
712 hydrothermal flow along mid-ocean ridges.

Acknowledgment

We gratefully acknowledge the Alvin Group and the captain and crew of the Atlantis II for their excellent work at sea. We also thank Jeff Seewald for fluid analysis using ion-chromatography and Lary Ball and Dave Schneider for access to the Plasma Mass Spectrometry Facility. We thank Brandy Toner for help with sample preparation and discussions. Support for W. Bach and K. Edwards was provided by NSF grant OCE-0241791 and support for O. Rouxel was provided by funding from the WHOI Deep Ocean Exploration Institute and NSF grant OCE-0622982 and OCE-0647948. We thank David Borrok, Kevin Mandernack, David Rickard two anonymous reviewers for helpful comments on the manuscript.

REFERENCES

Arnold, G.L., Weyer, S. and Anbar, A.D., 2004. Fe Isotope variations in natural materials measured using high mass resolution multiple collector ICPMS. Analytical Chemistry, 76, 322-327.

Auclair, G., Fouquet, Y. and Bohn, M., 1987. Distribution of Selenium in high-Temperature hydrothermal sulfide deposits at 13°N, East Pacific Rise. Canadian Mineralogist, 25, 577-587.

Beard, B.L., Johnson, C.M., Skulan, J.L., Nealson, K.H., Cox, L. and Sun, H., 2003a. Application of Fe isotopes to tracing the geochemical and biological cycling of Fe. Chemical Geology, 195, 87-117.

Beard, B.L., Johnson, C.M., VonDamm, K.L. and Poulson, R.L., 2003b. Iron isotope constraints on Fe cycling and mass balance in oxygenated Earth oceans. Geology, 31, 629-632.

Bluth, G.J. and Ohmoto, H., 1988. Sulfide-sulfate chimneys on the East Pacific Rise, 11° and 13°N latitudes. Part II: sulfur isotopes. Canadian Mineralogist, 26, 505-515.

Butler, I.B., Archer, C., Vance, D., Oldroyd, A. and Rickard, D., 2005. Fe isotope fractionation on FeS formation in ambient aqueous solution. Earth and Planetary Science Letters, 236, 430-442.

Chu, N.-C., Johnson, C.M., Beard, B.L., German, C.R., Nesbitt, R.W., Frank, M., Bohn, M., Kubik, P.W., Usui, A. and Graham, I., 2006. Evidence for hydrothermal venting in Fe isotope compositions of the deep Pacific Ocean through time. Earth and Planetary Science Letters, 245, 202-217.

Cowper, M. and Rickard, D., 1989. Mechanism of chalcopyrite formation from iron monosulphides in aqueous solutions (< 100°C, pH 2–4.5). Chemical Geology, 78, 325-341.

Dauphas, N. and Rouxel, O., 2006. Mass spectrometry and natural variations of iron isotopes. Mass Spectrometry Reviews, 25, 515-550.

Detrick, R.S., Buhl, P., Vera, E., Mutter, J., Orcutt, J., Madsen, J. and Brocher, T., 1987. Multi-channel seismic imaging of a crustal magma chamber along the East Pacific Rise. Nature, 326, 35-41.

Edmond, J.M., Campbell, A.C., Palmer, M.R., Klinkhammer, G.P., German, C.R., Edmonds, H.N., Elderfield, H., Thompson, G. and Rona, P., 1995. Time series studies of vent fluids from the TAG and MARK sites (1986, 1990) Mid-Atlantic Ridge: a new solution chemistry model and mechanism for Cu/Zn zonation in massive sulphide orebodies. In: L.M. Parson, C.L. Walker and D.R. Dixon (Editors), Hydrothermal Vents and Processes. Geological Society Special Publication, pp. 77-86.

Edmond, J.M., Measures, C., McDuff, R.E., Chan, L.H., Collier, R., Grant, B., Gordon, L.I. and Corliss, J.B., 1979. Ridge crest hydrothermal activity and the balances of the major and minor elements in the ocean: the Galapagos data. Earth and Planetary Science Letters, 46, 1-18.

Elderfield, H. and Schultz, A., 1996. Mid-ocean ridge hydrothermal fluxes and the chemical composition of the ocean. Annual Review of Earth and Planetary Sciences, 24, 191-224.

Fornari, D.J. and al, e., 1998. Axial summit trough of the East Pacific Rise 9°–10°N: Geological characteristics and evolution of the axial zone on fast spreading mid-ocean ridges. Journal of Geophysical Research, 103(B5), 9827-9856.

Fornari, D.J., Shank, T., VonDamm, K.L., Gregg, T.K.P., Lilley, M., Levai, G., Bray, A., Haymon, R.M., Perfit, M.R. and Lutz, R., 1998. Time-series temperature measurements at high-temperature hydrothermal vents, East Pacific Rise 9°49'-51'N: evidence for monitoring a crustal cracking event. Earth and Planetary Science Letters, 160, 419-431.

771 Fouquet, Y., 1997. Where are the large hydrothermal sulphide deposits in the oceans. Phil. Trans.
772 R. Soc. Lond., 355, 427-441.
773 Fouquet, Y., Auclair, G., Cambon, P. and Etoubleau, J., 1988. Geological setting and
774 mineralogical and geochemical investigations on sulfide deposits near 13°N on the East
775 Pacific Rise. Marine Geology, 84, 145-178.
776 Fouquet, Y., Knott, R., Cambon, P., Fallick, A., Rickard, D. and Desbruyeres, D., 1996.
777 Formation of large sulfide mineral deposits along fast spreading ridges; example from
778 off-axial deposits at 12 degrees 43'N on the East Pacific Rise. Earth and Planetary
779 Science Letters, 144, 147-162.
780 Hannington, M.D., Jonasson, I.R., Herzig, P.M. and Peterson, S., 1995. Physical and Chemical
781 Processes of Seafloor Mineralization at Mid-Ocean Ridges. In: S.E. Humphris, R.A.
782 Zierenberg, L.S. Mullineaux and R.E. Thomson (Editors), Seafloor hydrothermal
783 Systems: Physical, Chemical, Biological, and Geological Interactions. American
784 Geophysical Union, pp. 115-157.
785 Haymon, R.M., Fornari, D.J., Damm, K.L.V., Lilley, M.D., Perfit, M.R., Edmond, J.M., Shanks,
786 W.C., Lutz, R.A., Grebmeier, J.M., Carbotte, S., Wright, D., McLaughlin, E., Smith, M.,
787 Beedle, N. and Olson, E., 1993. Volcanic eruption of the mid-ocean ridge along the East
788 Pacific Rise crest at 9°45–52?N: Direct submersible observations of seafloor phenomena
789 associated with an eruption event in April, 1991. Earth and Planetary Science Letters,
790 119, 85-101.
791 Haymon, R.M., Fornari, D.J., Edwards, M.H., Carbotte, S., Wright, D. and Macdonald, K.C.,
792 1991. Hydrothermal vent distribution along the East Pacific Rise crest (9'09-54N) and its
793 relationship to magmatic and tectonic processes on fast-spreading mid-ocean ridges.
794 Earth and Planetary Science Letters, 104, 513-534.
795 Humphris, S.E., Herzig, P.M., Miller, D.J., Alt, J.C., Becker, K., Brown, D., Bruegmann, G.,
796 Chiba, H., Fouquet, Y., Gemmell, J.B., Guerin, G., Hannington, M.D., Holm, N.G.,
797 Honnorez, J.J., Iturrino, G.J., Knott, R., Ludwig, R., Nakamura, K., Petersen, S.,
798 Reysenbach, A.L., Rona, P.A., Smith, S., Sturz, A.A., Tivey, M.K. and Zhao, X., 1995.
799 The internal structure of an active sea-floor massive sulphide deposit. Nature, 377, 713-
800 716.
801 Janecky, D.R. and Shanks, W.C., 1988. Computational modeling of chemical and sulfur isotopic
802 reaction processes in seafloor hydrothermal systems: chimneys, massive sulfides, and
803 subjacent alteration zones. Can. Mineral., 26, 805-825.
804 John, S.G., Rouxel, O.J., Craddock, P.R., Engwall, A.M. and Boyle, E.A., 2008. Zinc stable
805 isotopes in seafloor hydrothermal vent fluids and chimneys. Earth and Planetary Science
806 Letters, doi: 10.1016/j.epsl.2007.12.011.
807 Kerridge, J.F., Haymon, R.M. and Kastner, M., 1983. Sulfur isotope systematics at the 21°N site,
808 East Pacific Rise. Earth and Planetary Science Letters, 66, 91-100.
809 Le Bris, N., Govenar, B., LeGall, C. and Fisher, C.R., 2006. Variability of physico-chemical
810 conditions in 9º50'N EPR diffuse flow vent habitats. Marine Chemistry, 98, 167-182.
811 Luther III, G.W., Rozan, T.F., Taillefert, M., Nuzzio, D.B., Meo, C.D., Shank, T.M., Lutz, R.A.
812 and Cary, S.C., 2001. Chemical speciation drives hydrothermal vent ecology. Nature,
813 410, 813-816.
814 Malinovski, D., Stenberg, A., Rodushkin, I., Andren, H., Ingri, J., Ohlander, B. and Baxter, D.C.,
815 2003. Performance of high resolution MC-ICPMS for Fe isotope ratio measurements in
816 sedimentary geological materials. Journal of Analytical Atomic Spectrometry, 18, 687-
817 695.
818 McManus, J., Nagler, T., Siebert, C., Wheat, C.G. and Hammond, D.E., 2002. Oceanic
819 molybdenum isotope fractionation; Diagenesis and hydrothermal ridge-flank alteration.
820 G, 3, doi:10.1029/2002GC000356.

Metz, S. and Trefry, J.H., 2000. Chemical and mineralogical influences on concentrations of trace metals in hydrothermal fluids. Geochimica et Cosmochimica Acta, 64, 2267-2279.
Ohmoto, H. and Goldhaber, M.B., 1997. Sulfur and Carbon isotopes. In: H.L. Barnes (Editor), Geochemistry of hydrothermal ore deposits Third Edition. Wiley, New York, pp. 517-611.
Ono, S., ShanksIII, W.C., Rouxel, O.J. and Rumble, D., 2007. Multiple-sulfur isotope constraints on the seawater sulfate contribution in modern seafloor hydrothermal sulfide. Geochem. Cosmochim. Acta, 71, 1170-1182.
Peng, X. and Zhou, H., 2005. Growth history of hydrothermal chimneys at EPR 9-10ºN: A structural and mineralogical study. Science in China Ser. D Earth Sciences, 48, 1891-1899.
Perfit, M.R., Fornari, D.J., Smith, M.C., Bender, J.F., Langmuir, C.H. and Haymon, R.M., 1994. Small-scale spatial ad temporal variations in mid-ocean ridge crest magmatic processes. Geology, 22, 375-379.
Poitrasson, F. and Freydier, R., 2005. Heavy iron isotope composition of granites determined by high resolution MC-ICP-MS. Chemical Geology, 222, 132-147.
Polyakov, V.B., 1997. Equilibrium fractionation of the iron isotopes: estimation from Mössbauer spectroscopy data. Geochimica et Cosmochimica Acta, 61, 4213-4217.
Polyakov, V.B., Clayton, R.N., Horita, J. and Mineev, S.D., 2007. Equilibrium iron isotope fractionation factors of minerals: Reevaluation from the data of nuclear inelastic resonant X-ray scattering and Mössbauer spectroscopy. Geochem. Cosmochim. Acta.
Polyakov, V.B. and Mineev, S.D., 2000. The use of Mössbauer spectroscopy in stable isotope geochemistry. Geochimica et Cosmochimica Acta, 64, 849-865.
Ravizza, G., Blusztajn, J., VonDamm, K.L., Bray, A.M., Bach, W. and Hart, S.R., 2001. Sr isotope variations in vent fluids from 9°46′-9°54′N East Pacific Rise: evidence of a non-zero-Mg fluid component. Geochimica et Cosmochimica Acta, 65, 729-739.
Rehkämper, M., Nielsen, S.G., Alt, J.C. and Butterfield, D.A., 2004. Thallium Isotope Constraints on Hydrothermal Water Fluxes at Mid-Ocean Ridge Axes and Flanks. Eos Trans. AGU, 85(47), Fall Meet. Suppl., Abstract V53B-06.
Rickard, D., 1997. Kinetics of pyrite formation by the H2S oxidation of iron (II) monosulfide in aqueous solutions between 25 and 125 C; the rate equation. Geochimica et Cosmochimica Acta, 61, 115–134.
Rouxel, O., Bekker, A. and Edwards, K., 2005. Iron Isotope Constraints on the Archean and Paleoproterozoic Ocean Redox State. Science, 307, 1088-1091.
Rouxel, O., Dobbek, N., Ludden, J. and Fouquet, Y., 2003a. Iron Isotope Fractionation During Oceanic Crust Alteration (Site ODP 801). Chemical Geology, 202, 155-182.
Rouxel, O., Fouquet, Y. and Ludden, J.N., 2004a. Copper Isotope systematics of the Lucky Strike, Rainbow and Logatchev Seafloor Hydrothermal Fields on the Mid Atlantic Ridge. Economic Geology, 99, 585-600.
Rouxel, O., Fouquet, Y. and Ludden, J.N., 2004b. Subsurface processes at the Lucky Strike hydrothermal field, mid-atlantic ridge: Evidence from sulfur, selenium and iron isotopes. Geochimica et Cosmochimica Acta, 68, 2295-2311.
Rouxel, O., Ludden, J. and Fouquet, Y., 2003b. Antimony isotope variations in natural systems and implications for their use as geochemical tracers. Chemical Geology, 200, 25-40.
Rouxel, O., Sholkovitz, E., Charette, M. and Edwards, K., 2007. Large Scale Iron Isotope Fractionation in Subterranean Estuaries. Geochem. Cosmochim. Acta (submitted).
Schauble, E.A., Rossman, G.R. and Taylor, H.P., 2001. Theoretical estimates of equilibrium Fe-isotope fractionations from vibrational spectroscopy. Geochimica et Cosmochimica Acta, 65, 2487-2497.

870 Schoonen, M.A.A. and Barnes, H.L., 1991. Reactions forming pyrite and marcasite from
871 solution: III. Hydrothermal processes. Geochimica et Cosmochimica Acta, 55, 3491-
872 3504.
873 Schouten, H., Tivey, M.A., Fornari, D.J. and Cochran, J.R., 1999. Central anomaly magnetization
874 high: constraints on the volcanic construction and architecture of seismic layer 2A at a
875 fast-spreading mid-ocean ridge, the EPR at 9°30′–50′N. Earth and Planetary Science
876 Letters, 169, 37-50.
877 Seewald, J.S. and Seyfried, W.E., 1990. The effect of temperature on metal mobility in
878 subseafloor hydrothermal systems: constraints from basalt alteration experiments. Earth
879 and Planetary Science Letters, 101, 388-403.
880 Severmann, S., Johnson, C.M., Beard, B.L., German, C.R., Edmonds, H.N., Chiba, H. and Green,
881 D.R.H., 2004. The effect of plume processes on the Fe isotope composition of
882 hydrothermally derived Fe in the deep ocean as inferred from the Rainbow vent site,
883 Mid-Atlantic Ridge, 36°14N. Earth and Planetary Science Letters, 225, 63-76.
884 Severmann, S., Johnson, C.M., Beard, B.L. and McManus, J., 2006. The effect of early diagenesis
885 on the Fe isotope compositions of porewaters and authigenic minerals in continental
886 margin sediments. Geochimica et Cosmochimica Acta, 70, 2006-2022.
887 Shank, T.M., Fornari, D.J., Damm, K.L.V., Lilley, M.D., Haymon, R.M. and Lutz, R.A., 1998.
888 Temporal and spatial patterns of biological community development at nascent deep-sea
889 hydrothermal vents (9'50N, East Pacific Rise). Deep-Sea Res.II, 45, 465-515.
890 Shanks, W.C., 2001. Stable isotopes in seafloor hydrothermal systems: vent fluids, hydrothermal
891 deposits, hydrothermal alteration, and microbial processes. Reviews in Mineralogy and
892 Geochemistry, 43, 469-525.
893 Shanks, W.C., Böhlke, J.K. and Seal, R.R., 1995. Stable Isotopes in Mid-Ocean Ridge
894 Hydrothermal Systems: Interactions between Fluids, Minerals, and Organisms. In: S.E.
895 Humphris, R.A. Zierenberg, L.S. Mullineaux and R.E. Thomson (Editors), Seafloor
896 Hydrothermal System: Physical, Chemical, Biological and Geological Ineractions, pp.
897 194-221.
898 Shanks, W.C. and Seyfried, W.E., 1987. Stable Isotope of Vent Fluids and Chimney Minerals,
899 Southern Juan de Fuca Ridge: Sodium Metasomatism ans Seawater Sulfate Reduction.
900 Journal of Geophysical Research, 92, 11387-11399.
901 Sharma, M., Polizzotto, M. and Anbar, A.D., 2001. Iron isotopes in hot springs along the Juan de
902 Fuca Ridge. Earth and Planetary Sciences Letters, 194, 39-51.
903 Tivey, M.K., 1995a. The influence of hydrothermal fluid composition and advection rates on
904 black smoker chimney mineralogy: Insights from modeling transport and reaction.
905 Geochimica et Cosmochimica Acta, 59, 1933-1949.
906 Tivey, M.K., 1995b. Modeling Chimney Growth and Associated Fluid Flow at Seafloor
907 Hydrothermal Vent Sites. In: S.E. Humphris, R.A. Zierenberg, L.S. Mullineaux and R.E.
908 Thomson (Editors), Seafloor hydrothermal Systems: Physical, Chemical, Biological, and
909 Geological Interactions. American Geophysical Union, pp. 158-177.
910 Tivey, M.K., Humphris, S.E., Thompson, G., Hannington, M.D. and Rona, P.A., 1995. Deducing
911 patterns of fluid flow and mixing within the TAG active hydrothermal mound using
912 mineralogical and geochemical data. Journal of Geophysical Research, 100, 12527-
913 12555.
914 Tivey, M.K., Stakes, D.S., Cook, T.L., Hannington, M.D. and Petersen, S., 1999. A model for
915 growth of steep-sided vent structures on the Endeavour Segment of the Juan de Fuca
916 Ridge: Results of a petrologic and geochemical study Journal of Geophysical Research
917 B: Solid Earth, 104 (B10), 22859-22883.
918 Von Damm, K.L., 1995. Controls on the Chemistry and Temporal Variability of Seafloor
919 Hydrothermal Fluids. In: S.E. Humphris, R.A. Zierenberg, L.S. Mullineaux and R.E.

Thomson (Editors), Seafloor hydrothermal Systems: Physical, Chemical, Biological, and Geological Interactions. American Geophysical Union, pp. 222-247.

Von Damm, K.L., 2000. Chemistry of hydrothermal vent fluids from 9°–10°N, East Pacific Rise: "Time zero," the immediate posteruptive period. J. Geophys. Res, 105, 11203-11222.

Von Damm, K.L., 2004. Evolution of the hydrothermal system at East Pacific Rise 9'50N: Geochemical evidence for changes in the upper oceanic crust. In: W.S.D. Wilcock, E.F. DeLong, D.S. Kelley, J.A. Baross and S.C. Cary (Editors), The subsurface biosphere at mid-ocean ridges, AGU Monograph 144.

Von Damm, K.L., Buttermore, L.G., Oosting, S.E., Bray, A.M., Fornari, D.J., Lilley, M.D. and Shanks, W.C., 1997. Direct observation of the evolution of a seafloor 'black smoker' from vapor to brine. Earth and Planetary Science Letters, 149, 101-111.

Von Damm, K.L., Edmond, J.M., Grant, B., Measures, C.I., Walden, B. and Weiss, R.F., 1985. Chemistry of submarine hydrothermal solutions at 21°N, East Pacific Rise. Geochimica et Cosmochimica Acta, 49, 2197-2220.

Von Damm, K.L. and Lilley, M.D., 2004. Diffuse flow hydrothermal fluids from 9'50N East Pacific Rise: Origin, evolution and biogeochemical controls. In: W.S.D. Wilcock, E.F. DeLong, D.S. Kelley, J.A. Baross and S.C. Cary (Editors), The subsurface biosphere at mid-ocean ridges, AGU Monograph 144, pp. 243-266.

Weyer, S. and Schwieters, J.B., 2003. High precision Fe isotope measurements with high mass resolution MC-ICPMS. International Journal of Mass Spectrometry, 226, 355-368.

Wilkin, R.T. and Barnes, H.L., 1996. Pyrite formation by reactions of iron monosulfides with dissolved inorganic and organic sulfur species. Geochimica et Cosmochimica Acta, 60, 4167–4179.

Woodruff, L.G. and Shanks, W.C., 1988. Sulfur Isotope Study of Chimney Minerals and Vent Fluids From 21°N, East Pacific Rise: Hydrothermal Sulfur Sources and Disequilibrium Sulfate Reduction. Journal of Geophysical Research, 93, 4562-4572.

Yamamoto, M., Kase, K. and Ueda, A., 1983. Fractionation of sulfur isotopes and selenium between coexisting pyrite and chalcopyrite from the Hitachi deposits, Ibaraki Prefecture, Japan. Geochem. J., 17, 29-39.

Zhu, X.K., O'Nions, R.K., Guo, Y., Belshaw, N.S. and Rickard, D., 2000. Determination of natural Cu-isotope variation by plasma-source mass spectrometry: implications for use as geochemical tracers. Chemical Geology, 163, 139-149.

954 **Figure Captions**

955

956 **Figure 1:** Location map of known hydrothermal vents in the 9º50'N area superimposed onto the
957 ABE microbathymetry map (depth in meters). Only sites sampled for this study are labeled.

958

959 **Figure 2:** Seafloor digital photographs of active chimneys K-vent and Bio 9" and inactive
960 chimney and massive sulfide deposits. (a) The spire at K-vent is composed of a diffuser with
961 numerous little vents that emanate clear fluid and is colonized by *Alvinella,* sea anemones and
962 vent grabs. Sample ALV-4053-M1 is from the ~1m long chimney growing on the upper part of
963 the spire. (b) The hydrothermal chimney at Bio9'' is venting vigorously at a temperature of
964 383ºC. Sample ALV-4057-M1 represents the uppermost 40-50 cm of the entire black smoker. (c)
965 Sample ALV-4057-M2 is from an extinct sulfide structure just north of Bio9''. Relics of a central
966 vent conduit lined with marcasite and sphalerite suggest that this sample could be related to a Zn-
967 rich diffuser vent-type. (d) Sample ALV-4059-M2 is from an extinct sulfide structure covered by
968 an extensive Fe-oxide crust. The lack of distinct chimney structure suggests that these Fe-rich
969 massive sulfides formed from late-stage remineralization of collapsed chimney fragments at the
970 seafloor.

971

972 **Figure 3:** Photomosaics of sample ALV-4053-M1 from K-vent and sample ALV-4057-M1 from
973 Bio-9''. Red lines and labels mark subsamples for chemical and isotope analysis. See text for a
974 detailed description.

975

976 **Figure 4:** Diagram showing the distribution of δ^{56}Fe in vent fluids and sulfides (chalcopyrite,
977 pyrite, marcasite and sphalerite) at EPR 9-10°N compared with literature and unpublished data
978 for other vent fields along Mid-Atlantic Ridge. References : (a) Beard et al. (2003b); (b) Rouxel
979 et al. (2004b); (c) this study; (d) Severmann et al. (2004); (e) Rouxel, unpublished data (samples
980 from Rouxel et al. (2004a). Light grey bar represents the bulk Earth isotopic composition
981 estimated from the composition of igneous rocks (Beard et al., 2003a; Dauphas and Rouxel,
982 2006).

983

984 **Figure 5:** δ^{56}Fe *vs* Fe/Mn ratios and Na concentration for hydrothermal fluid end-members (open
985 circle) and insoluble fluid particles (dregs or >0.4μm particles). Data sources and references are
986 presented in **Table 2**. Vent name, fluid temperature and year of sampling are shown. Gray

horizontal line represents igneous rocks (MORB) isotope composition (Beard et al., 2003a; Dauphas and Rouxel, 2006). Paired fluid-particles are joined by solid lines for each vent.

Figure 6: Comparison of $\delta^{56}Fe$ and $\delta^{34}S$ values of sulfide minerals lining chimney walls at Bio9" and K-vent (pyrite, marcasite and chalcopyrite) with $\delta^{56}Fe$ and $\delta^{34}S$ values of the vent fluids. Dark solid lines correspond to the calculated equilibrium isotope fractionation factors ($\Delta^{56}Fe$ and $\Delta^{34}S$) between pyrite and Fe^{2+} and H_2S respectively. $\Delta^{56}Fe(FeS_2\text{-}Fe^{2+})$ and $\Delta^{34}S(FeS_2\text{-}H_2S)$ are calculated at 350°C after Ohmoto and Goldhaber (1997), Polyakov and Mineev (2000) and Schauble et al. (2001). Gray line corresponds to equilibrium S-isotope fractionation factor between chalcopyrite and H_2S at 350°C (Ohmoto and Goldhaber, 1997). Dash line correspond to the maximum kinetic Fe-isotope fractionation factors during FeS (mackinawite) precipitation from Fe^{2+}-rich aqueous solutions at ambient temperatures (Butler et al., 2005).

Figure 7: $\delta^{56}Fe$ *vs* $\delta^{34}S$ plots for chalcopyrite (cpy, triangle), marcasite-pyrite (mar-py, square) and sphalerite-rich sulfides (sph-py diamond). Fe- and S-isotope compositions of all end-member hydrothermal fluids at EPR 9-10°N are also shown for comparisons (Hyd. Fluid, circle). Samples are grouped together using solid lines when they are in close association (i.e. coexisting) to each other. For example, chalcopyrite lining chimney wall at Bio9'' is paired with hydrothermal fluids but also with pyrite-marcasite that occur outside the chimney wall. When marcasite and sphalerite at K-vent is recovered from the internal lining of the chimney, they are also referred as paired.

Figure 8: Schematic illustration of an idealized hydrothermal deposit, including massive sulfide mound with stockwork root zone (dark gray area) growing on volcanic rock substrate (light gray area). Emission of both high-temperature (350°C) (black arrow) and lower temperature (200-250°C) fluids through black smoker and diffusers (gray arrow), as well as diffuse, low-temperature fluid (<100°C) (dashed arrows) are also illustrated. Pathways or hydrothermal fluid flows which affect Fe-isotopes in both sulfides and fluids are also presented. (1) Direct venting of the hydrothermal fluid at seafloor will produce pyrite-rich chimneys with low $\delta^{56}Fe$ and $\delta^{34}S$ values while chalcopyrite will have $\delta^{56}Fe$ values (and to a lesser extent $\delta^{34}S$ values) close to fluid composition. (2) Cooling of the hydrothermal fluid in subsurface environments will produce massive sulfides (noted as crossed lines in the figure) with minimal Fe-isotope fractionation, leaving lower temperature fluids with essentially the same $\delta^{56}Fe$ and $\delta^{34}S$ values than high-temperature vents. Remineralization of previously precipitated sulfides by late-stage fluids may

also produce massive sulfides with minimal Fe- and S-isotope fractionation relative to hydrothermal fluids. (3) Circulation of seawater through altered substratum may mixed with hydrothermal fluids and produce warm fluids with more variable Fe-isotope composition due to rapid sulfide precipitation (i.e. increase of δ^{56}Fe values) or basalt alteration and partial Fe-oxidation (i.e. decrease of δ^{56}Fe values).

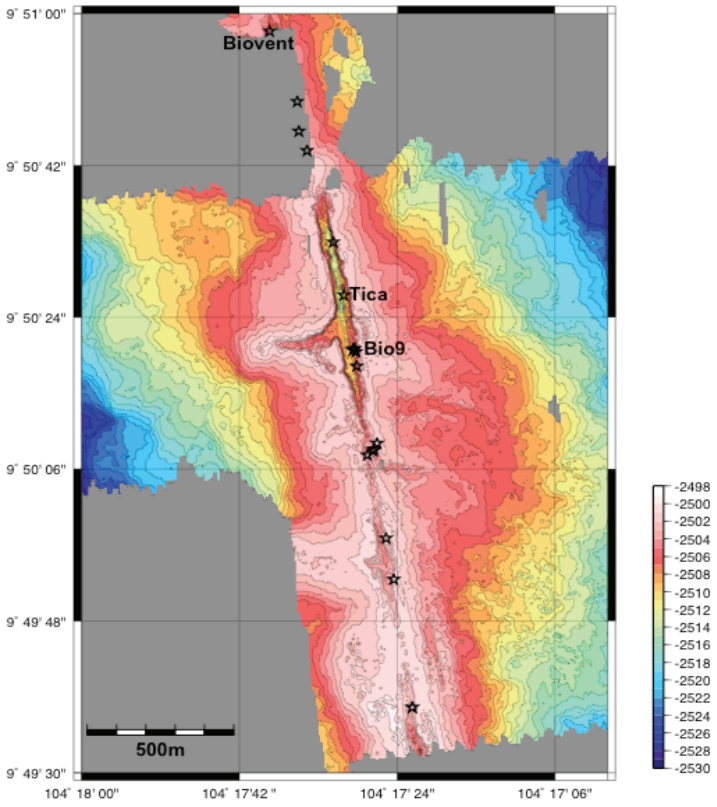
9° 51' 00"
9° 50' 42"
9° 50' 24"
9° 50' 06"
9° 49' 48"
9° 49' 30"
104° 18' 00"
104° 17'42 "
104° 17' 24"
104° 17' 06"
Biovent
Tica
Bio9
500m
-2498
-2500
-2502
-2504
-2506
-2508
-2510
-2512
-2514
-2516
-2518
-2520
-2522
-2524
-2526
-2528
-2530

Figure 1

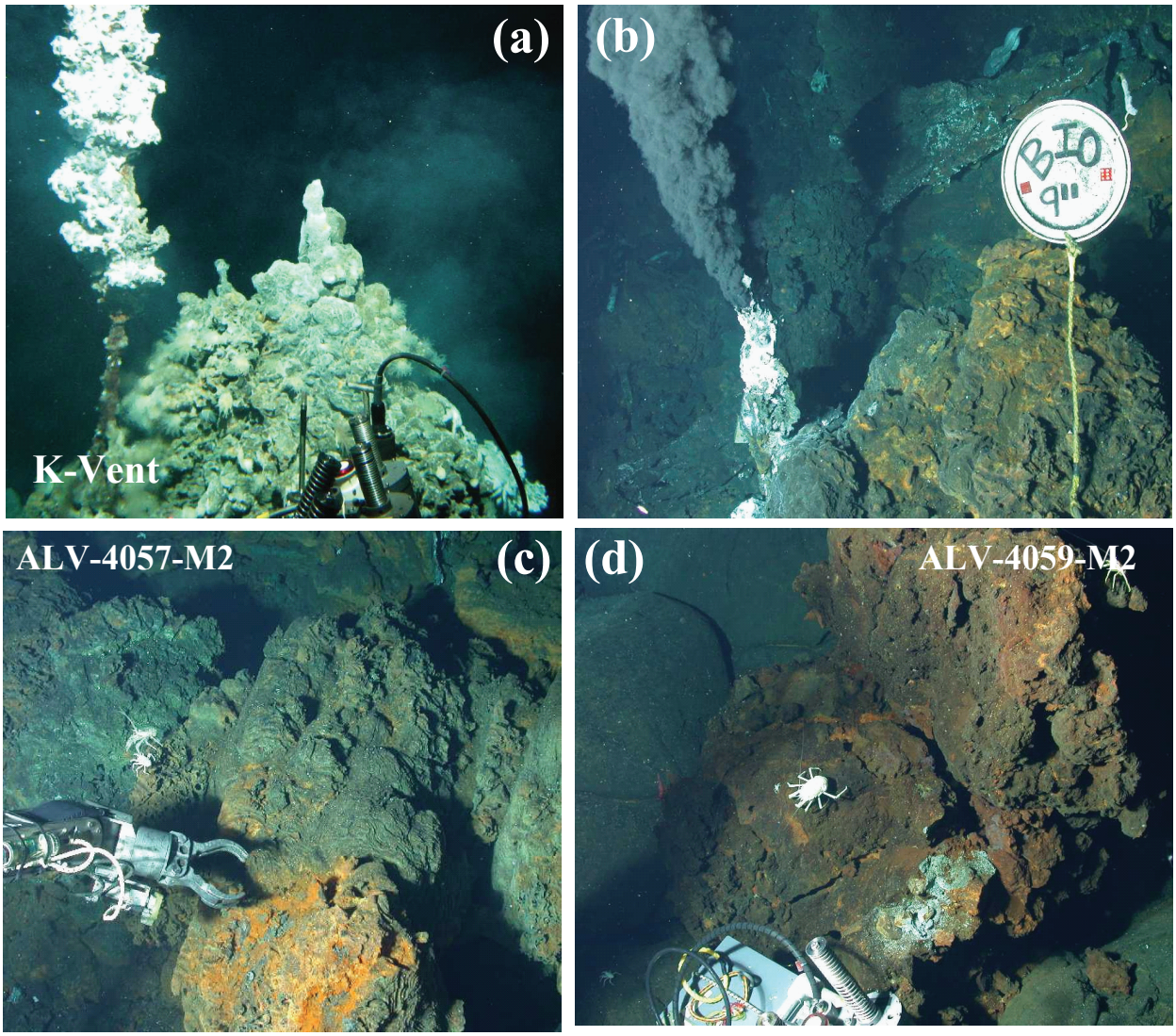

Figure 2

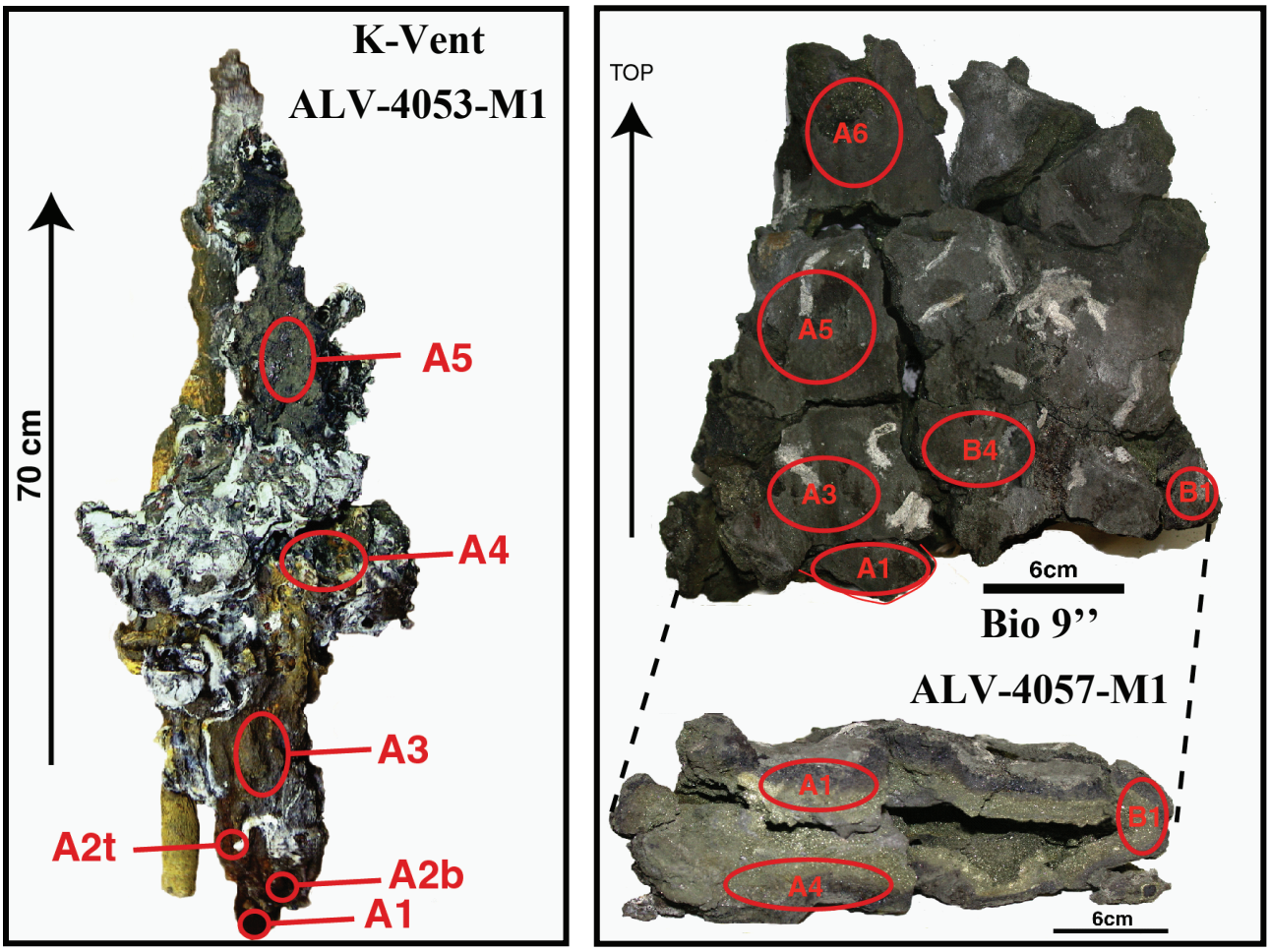
K-Vent
ALV-4053-M1
70 cm
A5
A4
A3
A2t
A2b
A1
TOP
A6
A5
B4
A3
B1
A1
6cm
Bio 9''
ALV-4057-M1
A1
B1
A4
6cm

Figure 3

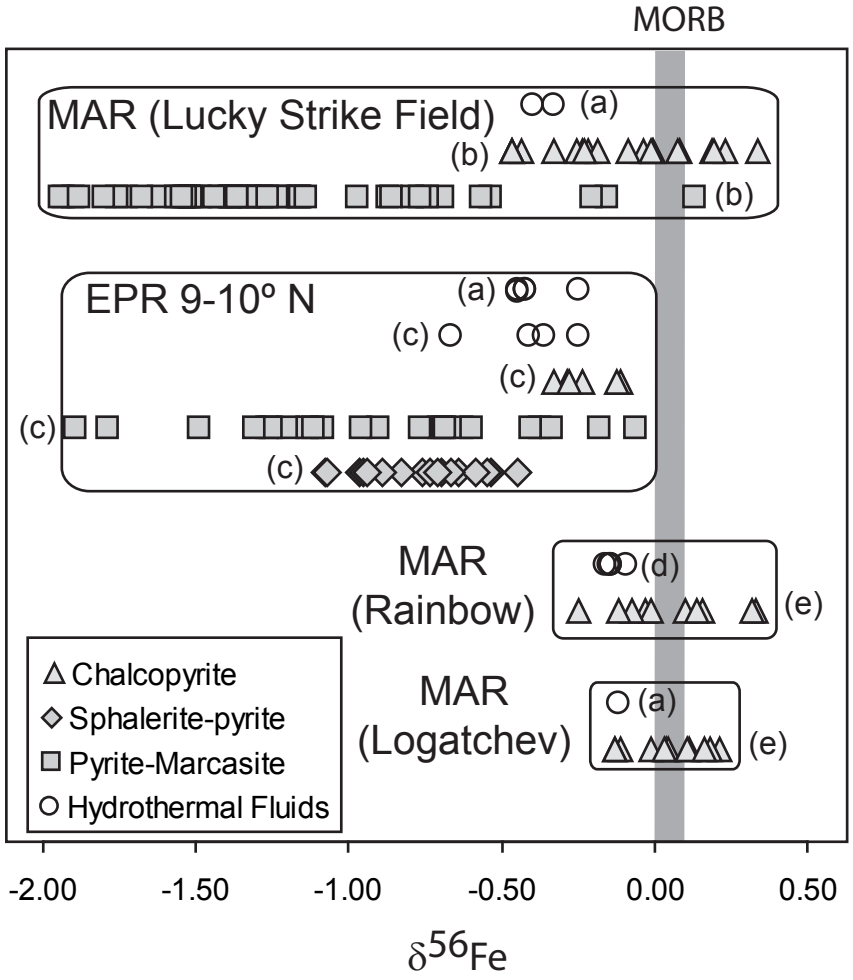
MORB
MAR (Lucky Strike Field)
(a)
(b)
(b)
EPR 9-10º N
(a)
(c)
(c)
(c)
(c)
MAR
(Rainbow)
(d)
(e)
MAR
(Logatchev)
(a)
(e)
Chalcopyrite
Sphalerite-pyrite
Pyrite-Marcasite
Hydrothermal Fluids
-2.00
-1.50
-1.00
-0.50
0.00
0.50
δ56Fe

Figure 4

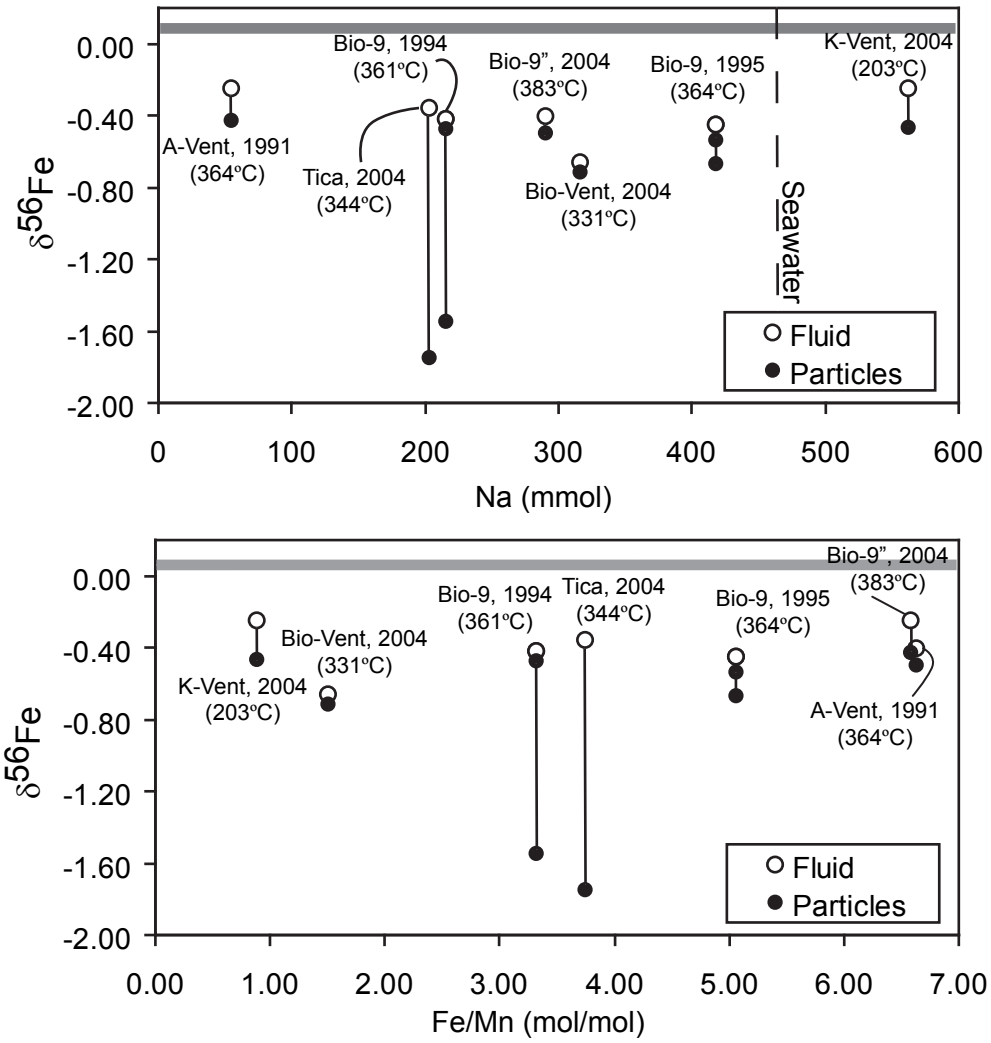
0.00
-0.40
-0.80
-1.20
-1.60
-2.00
δ56Fe
0
100
200
300
400
500
600
Na (mmol)
A-Vent, 1991
(364ºC)
Bio-9, 1994
(361ºC)
Tica, 2004
(344ºC)
Bio-9”, 2004
(383ºC)
Bio-Vent, 2004
(331ºC)
Bio-9, 1995
(364ºC)
Seawater
K-Vent, 2004
(203ºC)
Fluid
Particles
0.00
-0.40
-0.80
-1.20
-1.60
-2.00
δ56Fe
0.00
1.00
2.00
3.00
4.00
5.00
6.00
7.00
Fe/Mn (mol/mol)
Bio-9”, 2004
(383ºC)
Bio-9, 1994
(361ºC)
Tica, 2004
(344ºC)
Bio-9, 1995
(364ºC)
Bio-Vent, 2004
(331ºC)
K-Vent, 2004
(203ºC)
A-Vent, 1991
(364ºC)
Fluid
Particles

Figure 5

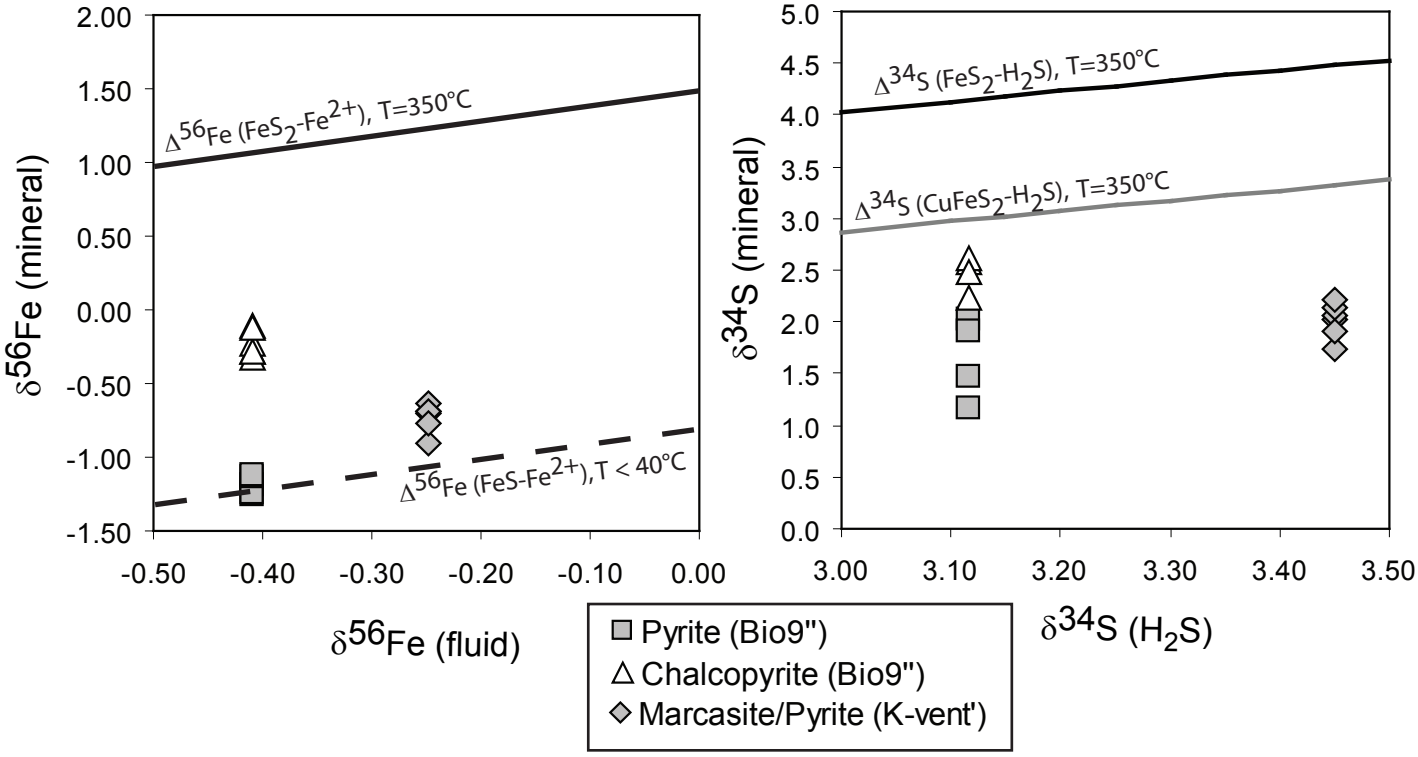
2.00
1.50
1.00
0.50
0.00
-0.50
-1.00
-1.50
δ56Fe (mineral)
Δ56Fe (FeS2-Fe2+), T=350°C
Δ56Fe (FeS-Fe2+), T < 40°C
-0.50
-0.40
-0.30
-0.20
-0.10
0.00
δ56Fe (fluid)
5.0
4.5
4.0
3.5
3.0
2.5
2.0
1.5
1.0
0.5
0.0
δ34S (mineral)
Δ34S (FeS2-H2S), T=350°C
Δ34S (CuFeS2-H2S), T=350°C
3.00
3.10
3.20
3.30
3.40
3.50
δ34S (H2S)
Pyrite (Bio9")
Chalcopyrite (Bio9")
Marcasite/Pyrite (K-vent')

Figure 6

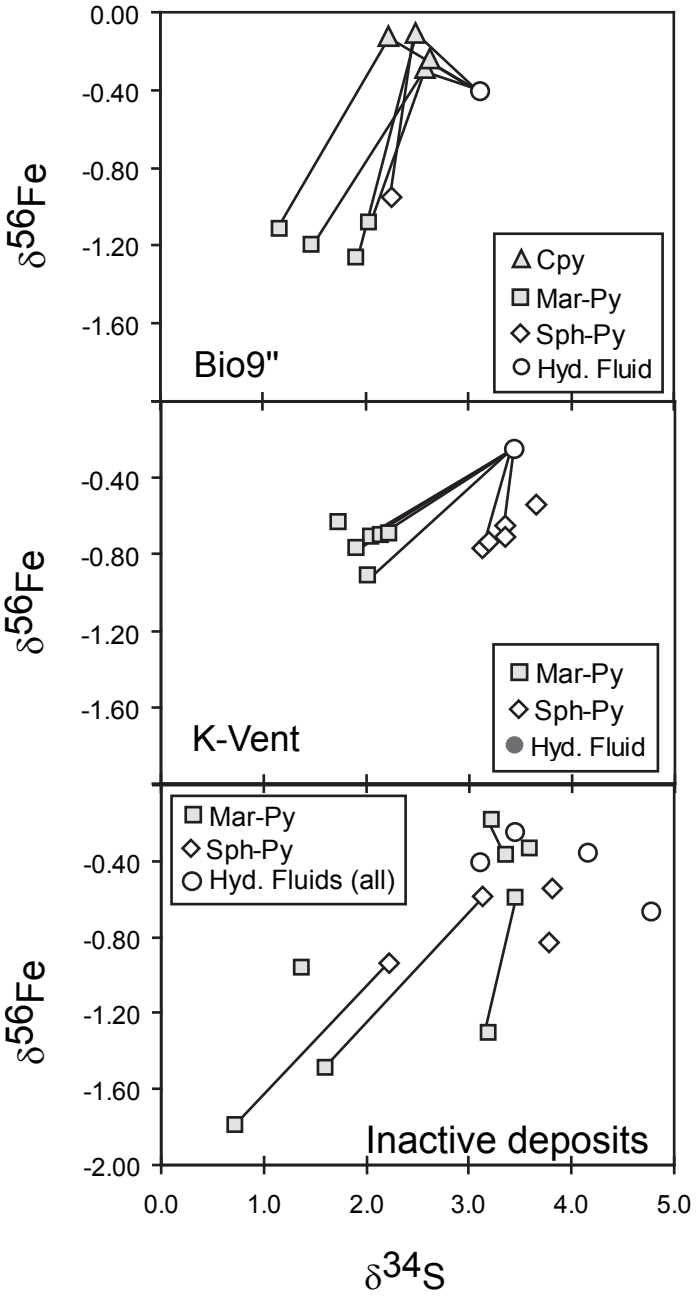
0.00
-0.40
-0.80
-1.20
-1.60
δ56Fe
Bio9"
Cpy
Mar-Py
Sph-Py
Hyd. Fluid
-0.40
-0.80
-1.20
-1.60
δ56Fe
K-Vent
Mar-Py
Sph-Py
Hyd. Fluid
Mar-Py
Sph-Py
Hyd. Fluids (all)
-0.40
-0.80
-1.20
-1.60
-2.00
δ56Fe
Inactive deposits
0.0
1.0
2.0
3.0
4.0
5.0
δ34S

Figure 7

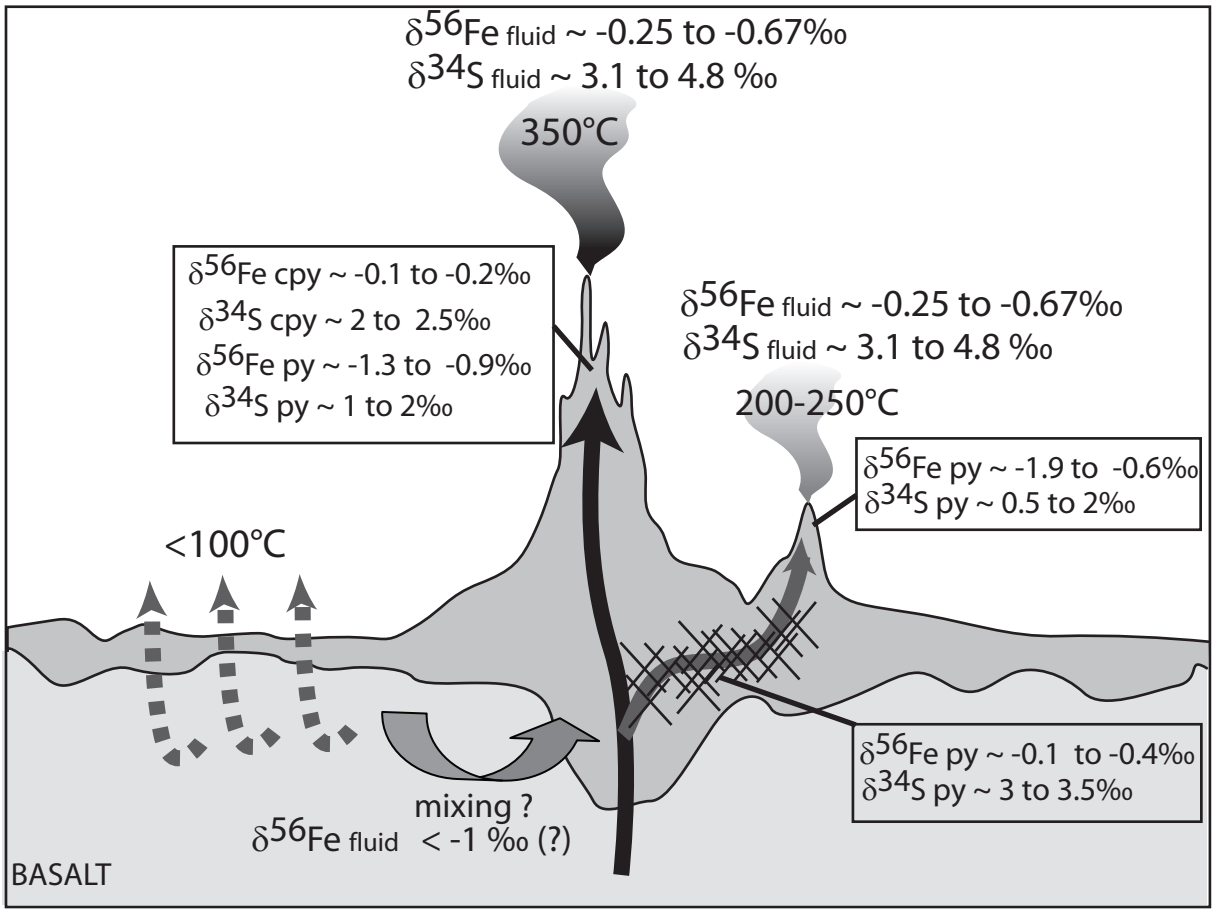
δ56Fe fluid ~ -0.25 to -0.67‰
δ34S fluid ~ 3.1 to 4.8 ‰
350°C
δ56Fe cpy ~ -0.1 to -0.2‰
δ34S cpy ~ 2 to 2.5‰
δ56Fe py ~ -1.3 to -0.9‰
δ34S py ~ 1 to 2‰
δ56Fe fluid ~ -0.25 to -0.67‰
δ34S fluid ~ 3.1 to 4.8 ‰
200-250°C
δ56Fe py ~ -1.9 to -0.6‰
δ34S py ~ 0.5 to 2‰
<100°C
δ56Fe py ~ -0.1 to -0.4‰
δ34S py ~ 3 to 3.5‰
mixing ?
δ56Fe fluid < -1 ‰ (?)
BASALT

Figure 8

Table 1: Temperature, pH and chemical and isotope composition of hydrothermal fluids and particles

Sample	T °C (a)	pH (25°C, 1atm)	Mg (mM)	Na (mM)	K (mM)	Ca (mM)	Fe (μM)	Mn (μM)	Cu (μM)	Zn (μM)	Pb (nM)	Co (nM)	$\delta^{34}S_{VCDT}$ vs	$\delta^{56}Fe$	1sd (d)	$\delta^{57}Fe$	1sd (d)
K-vent (9°29.7228; 104°14.4679)																	
ALV-4053-W1	203	4.53	8.2	541	25.3	22.3	170	191	0.10	1.46	99	<10	**3.6**	**-0.27**	0.07	**-0.30**	0.07
ALV-4053-W1/Dregs (b)						<0.005	5	0.12	0.23	0.59	15	<10		**-0.62**	0.08	**-0.90**	0.12
ALV-4053-W2	203	5.30	27.31	517.4	19.02	17.55	88	109	0.10	1.85	61	<10	**3.3**	**-0.21**	0.03	**-0.20**	0.04
ALV-4053-W2/Dregs (b)						<0.005	7	0.13	0.51	1.93	40	<10		**-0.33**	0.06	**-0.47**	0.04
Bio9" (9°50.2749; 104°17.4884)																	
ALV-4057-W1	383	3.21	5.3	307	10.8	11.9	3165	483	50.33	71.49	228	1052	**3.2**	**-0.43**	0.02	**-0.62**	0.02
ALV-4057-W1/Dregs (b)						<0.005	8	0.14	2.85	3.65	12	45		**-0.56**	0.02	**-0.77**	0.06
ALV-4057-W2	383	3.30	8.5	318	10.8	11.9	3045	461	45.79	53.55	170	909	**3.1**	**-0.38**	0.03	**-0.53**	0.07
ALV-4057-W2/Dregs (b)						<0.005	43	0.15	16.70	19.83	66	244		**-0.45**	0.04	**-0.64**	0.04
Tica Vent (9°50.4274; 104°17.494)																	
ALV-4059-W1	344	3.16	5.2	228	7.5	11.5	1365	377	8.45	40.97	84	<10	**4.2**	**-0.33**	0.09	**-0.46**	0.15
ALV-4059-W1/Dregs (b)						<0.005	52	0.23	2.98	14.14	37	28		**-1.71**	0.04	**-2.64**	0.04
ALV-4059-W2	344	3.13	7.2	238	7.6	11.1	1282	369	7.45	39.31	79	<10	**4.1**	**-0.22**	0.02	**-0.37**	0.05
ALV-4059-W2/Dregs (b)						<0.005	99	0.30	3.33	15.73	42	56		**-1.79**	0.02	**-2.67**	0.03
Biovent (9º50.9731 104º17.6275)																	
ALV-4061-W3	331	4.45	25.3	389	11.4	10.1	151	101	8.45	19.85	129	<10	**4.1**	**-0.64**	0.05	**-1.00**	0.13
ALV-4061-W3/Dregs (b)						<0.005	5	0.10	1.43	2.84	9	<10		**-0.72**	0.05	**-1.10**	0.02
ALV-4061-W4	331	3.79	4.3	320	12.3	9.5	264	180	12.34	27.00	166	<10	**5.4**	**-0.69**	0.08	**-0.97**	0.13
ALV-4061-W4/Dregs (b)						<0.005	1	0.10	0.59	1.11	5	<10		**-0.72**	0.11	**-1.09**	0.12
Seawater *(c)*			54.8	464	10.1	9.95	<1	0.01	<0.1	<0.1	<5	<10					

(a) Maximum temperature measured using ICL temperature probe prior fluid sampling

(b) Dregs: insoluble particles precipitated in the Ti-sampler used for hydrothermal fluid sampling

(c) Minimum concentrations correspond to the limit of determination

(d) the internal precision of Fe-isotope analysis are given as 1 standard deviation

Table 2: End-member and isotopic mass balance in hydrothermal fluids

Sample	Year Sampling	T (°C)	Na (mM)	K (mM)	Ca (mM)	Fe (μM)	Mn (μM)	Cu (μM)	Zn (μM)	Pb (nM)	Co (nM)	$\delta^{34}S_{vs\ VCDT}$	$\delta^{56}Fe$ (d)	$\delta^{56}Fe_p$ (e)	Fe/Mn
K-vent															
ALV-4053 (a)	2004	203	562	28	25	197	221	0.8	5.0	168	<50	3.45	**-0.25**	**-0.47**	0.89
2362 (K.1) (b)	1991	263	458	27.8	23	373	306	-	-	-	-				1.22
Bio9''															
ALV-4057 (a)	2004	383	291	11	12	3584	540	66	85	273	1290	3.12	**-0.41**	**-0.50**	6.63
Bio 9															
2735-4 (B9'.1) (b,c)	1994	361	216	8.67	9.8	1270	382	-	-	-	-		**-0.42**	**-0.48**	3.32
2735-4 (B9'.1) (c)	1994													**-1.55**	
3030-11 (B9.8) (b,c)	1995	364	418	14.7	24.6	6030	1190	-	-	-	-		**-0.45**	**-0.54**	5.07
3030-11 (B9.8) (c)	1995													**-0.67**	
Tica Vent															
ALV-4059 (a)	2004	344	204	7	11	1577	421	13	62	137	<50	4.16	**-0.36**	**-1.75**	3.75
Biovent															
ALV-4061 (a)	2004	331	316	13	10	289	192	16	36	222	<50	4.78	**-0.67**	**-0.72**	1.51
A-Vent															
2360-1C (Aa.1) (b,c)	1991	390	55.4	2.19	2	1560	237	-	-	-	-		**-0.25**	-0.43	6.58

(a) end-member chemical and Fe-isotopic composition calculated from table 1

(b) end-member chemical composition from Von Damm, 2000

(c) Fe-isotope composition from Beard et al., 2003

(d) end-member Fe-isotope composition (include dissolve and particles)

(e) average Fe-isotope composition of particulate Fe (DREGS or >0.4um particles)

Table 3: Chemical composition and sample description of mineral separates of active and inactive sulfide deposits

Sample Name	minerals (a)	Fe (wt%)	Cu (wt%)	Zn (wt%)	Ca (wt%)	Pb (wt%)	As (ppm)	Se (ppm)	$\delta^{34}S_{VCDT}$	$\delta^{56}Fe$	1sd (b)	$\delta^{57}Fe$	1sd (b)
Bio 9'' (Cu-rich chimneys)													
ALV-4057-M1 #A1	cpy	29.0	27.11	0.09	1.80	0.00	8	1,217	**2.6**	**-0.29**	0.05	**-0.34**	0.09
ALV-4057-M1 #A1	py	41.8	0.23	0.82	1.11	0.02	80	12	**2.0**	**-1.08**	0.01	**-1.62**	0.01
ALV-4057-M1 #A1	sph-py	26.3	0.59	22.67	0.02	0.07	207	71		**-1.08**	0.06	**-1.70**	0.07
ALV-4057-M1 #A3	cpy	29.3	29.09	0.15	0.05	0.00	13	1,206	**2.6**	**-0.24**	0.04	**-0.27**	0.04
ALV-4057-M1 #A3	py	41.3	0.13	0.94	0.06	0.05	148	7	**1.5**	**-1.20**	0.08	**-1.77**	0.10
ALV-4057-M1 #A3	sph-py	26.3	1.88	23.98	0.09	0.06	209	99		**-0.89**	0.03	**-1.32**	0.06
ALV-4057-M1 #A4	cpy	28.1	29.34	0.13	0.66	0.00	2	1,321	**2.5**	**-0.11**	0.14	**-0.13**	0.20
ALV-4057-M1 #A4	py	41.8	0.77	0.70	0.73	0.03	115	17	**1.9**	**-1.26**	0.02	**-1.94**	0.03
ALV-4057-M1 #A4	sph-py	21.1	2.32	26.51	0.03	0.06	200	145	**2.3**	**-0.95**	0.09	**-1.44**	0.13
ALV-4057-M1 #A5	cpy	26.5	27.32	0.04	0.94	0.00	1	1,321		**-0.33**	0.10	**-0.40**	0.08
ALV-4057-M1 #A5	py	39.4	3.24	0.95	0.01	0.04	135	146		**-1.25**	0.02	**-1.87**	0.03
ALV-4057-M1 #A5	sph-py	25.5	0.64	22.90	0.03	0.06	222	57		**-1.07**	0.07	**-1.73**	0.09
ALV-4057-M1 #A6	cpy	29.0	31.68	0.02	0.19	0.00	1	1,632		**-0.28**	0.12	**-0.46**	0.12
ALV-4057-M1 #A6	py	42.9	0.18	0.10	0.90	0.02	54	2		**-1.14**	0.05	**-1.72**	0.06
ALV-4057-M1 #B1	cpy	28.9	30.81	0.05	0.02	0.00	1	1,402	**2.2**	**-0.12**	0.01	**-0.24**	0.10
ALV-4057-M1 #B1	py	40.3	0.48	1.58	0.07	0.03	164	23	**1.2**	**-1.12**	0.04	**-1.71**	0.05
K-Vent (Active Fe-Zn-rich chimneys and diffusers)													
ALV-4053-M1 #A1	mar	38.1	1.11	1.12	0.03	1.17	2184	63	**2.0**	**-0.90**	0.03	**-1.34**	0.02
ALV-4053-M1 #A1	py-sph	16.6	0.31	8.17	0.94	4.61	851	27	**3.4**	**-0.64**	0.02	**-0.93**	0.06
ALV-4053-M1 #A1	sph-py-ga	10.6	1.16	24.82	0.67	12.26	380	112	**3.4**	**-0.70**	0.06	**-1.05**	0.08
ALV-4053-M1 #A2b	mar	39.6	1.18	0.63	0.07	0.72	2863	45	**2.1**	**-0.70**	0.06	**-0.97**	0.04
ALV-4053-M1 #A2b	py-sph	20.7	0.15	4.34	0.63	1.27	838	15	**3.7**	**-0.54**	0.05	**-0.78**	0.06
ALV-4053-M1 #A2b	sph-py-ga	10.2	0.69	20.88	0.04	15.87	644	81		**-0.67**	0.04	**-1.04**	0.05
ALV-4053-M1 #A2t	py	22.9	0.01	0.52	0.01	0.13	438	5	**2.1**	**-0.69**	0.06	**-0.99**	0.06
ALV-4053-M1 #A2t	sph-py-ga	9.7	0.16	8.90	0.00	4.38	249	19		**-0.71**	0.04	**-1.12**	0.08
ALV-4053-M1 #A3	py	17.0	0.01	1.38	0.04	0.53	455	14	**1.9**	**-0.77**	0.02	**-1.14**	0.05
ALV-4053-M1 #A4	py	31.7	0.01	0.66	0.02	0.31	612	3	**1.7**	**-0.63**	0.05	**-0.88**	0.04
ALV-4053-M1 #A4	py-sph	23.3	0.15	11.47	0.05	4.17	1034	26	**3.1**	**-0.76**	0.05	**-1.08**	0.05
ALV-4053-M1 #A5	py	22.5	0.02	1.47	0.01	0.66	823	4	**2.2**	**-0.69**	0.02	**-1.02**	0.01
ALV-4053-M1 #A5	py-sph	27.5	0.17	13.22	0.01	4.71	1018	27	**3.2**	**-0.73**	0.07	**-0.99**	0.08
Fe-Zn-rich inactive chimneys													
ALV-4053-M2-a	sph-cpy-mar	22.4	6.93	25.25	0.02	0.05	313	265		**-0.44**	0.09	**-0.65**	0.12
ALV-4053-M2-a	sph-mar	12.1	0.92	43.47	0.01	0.13	58	222	**3.8**	**-0.55**	0.07	**-0.88**	0.10
ALV-4053-M2-a	mar-sph	19.0	0.22	5.62	0.01	0.20	380	32		**-0.97**	0.01	**-1.35**	0.03
ALV-4053-M3	sph-py	16.0	0.40	28.44	0.01	0.73	205	65	**3.1**	**-0.59**	0.07	**-0.86**	0.09
ALV-4053-M3	py-mar	32.4	0.04	2.97	0.05	0.24	642	15	**1.4**	**-0.96**	0.07	**-1.49**	0.05
ALV-4057-M2	sph-py-mar	16.2	0.32	37.76	0.11	0.03	73	24	**2.2**	**-0.94**	0.10	**-1.37**	0.17
ALV-4057-M2	py-mar	41.4	0.01	0.87	0.01	0.05	358	10	**0.7**	**-1.79**	0.06	**-2.58**	0.01
ALV-4059-M3	sph	9.8	0.38	45.38	0.03	0.02	43	16	**3.8**	**-0.83**	0.02	**-1.17**	0.09
ALV-4059-M3#1	mar	39.3	0.17	1.55	0.01	0.04	213	74	**3.5**	**-0.60**	0.03	**-0.80**	0.02
ALV-4059-M3#2	mar	40.7	0.04	0.61	0.02	0.09	199	7	**3.2**	**-1.31**	0.00	**-1.89**	0.02
ALV-4059-M4#1	py	36.6	0.03	2.74	0.01	0.05	210	26	**1.6**	**-1.49**	0.03	**-2.33**	0.03
ALV-4059-M4#2	py	38.0	0.01	0.13	0.01	0.04	121	2		**-1.89**	0.06	**-2.94**	0.10
Fe-rich massive sulfides													
ALV-4058-M1-a	py	41.9	0.08	0.10	0.01	0.02	141	84	**3.2**	**-0.18**	0.03	**-0.16**	0.11
ALV-4058-M1-b#1	py	40.5	2.62	0.09	0.02	0.04	163	49	**3.4**	**-0.37**	0.06	**-0.46**	0.01
ALV-4058-M1-b#2	py	42.4	0.17	0.14	0.02	0.02	201	60		**-0.06**	0.07	**-0.09**	0.03
ALV-4059-M2-1	py	41.3	0.33	0.24	0.02	0.03	451	51	**3.6**	**-0.34**	0.00	**-0.43**	0.05
ALV-4059-M2-2	py	42.0	0.06	0.15	0.02	0.03	157	39		**-0.40**	0.11	**-0.53**	0.16

(a) mar: marcasite; py: pyrite; sph: sphalerite; cpy: chalcopyrite; ga: galena

(b) the internal precision of Fe-isotope analysis are given as 1 standard deviation

Table S1: Chemical composition and sample description of mineral separates of active and inactive sulfide deposits

Sample Name	mineral (a)	CaSO4 (b) (%)	CuFeS2 (c) (%)	ZnS (d) (%)	PbS (e) (%)	FeS2 (f) (%)	Sample Description
Bio 9" (Cu-rich chimneys)							
ALV-4057-M1 #A1	cpy	8.6	82.2	0.2	0.0	9.0	Euhedral to massive chalcopyrite with trace anh lining internal wall
ALV-4057-M1 #A1	py	3.5	0.5	1.6	0.0	94.4	Massive to fine-grained py aggregates from external wall
ALV-4057-M1 #A1	sph-py	0.1	1.2	44.0	0.0	54.7	Fine-grained sph+py aggregates inside chimney wall
ALV-4057-M1 #A3	cpy	0.2	95.7	0.5	0.0	3.6	Euhedral to massive chalcopyrite lining internal wall
ALV-4057-M1 #A3	py	0.2	0.3	1.9	0.0	97.6	Massive to fine-grained py aggregates from external wall
ALV-4057-M1 #A3	sph-py	0.3	3.7	45.5	0.0	50.4	Fine-grained sph+py aggregates inside chimney wall
ALV-4057-M1 #A4	cpy	3.4	96.2	0.4	0.0	0.0	Euhedral to massive chalcopyrite lining internal wall
ALV-4057-M1 #A4	py	2.3	1.6	1.4	0.0	94.7	Massive to fine-grained py aggregates from external wall
ALV-4057-M1 #A4	sph-py	0.1	4.9	54.5	0.0	40.5	Fine-grained sph+py aggregates inside chimney wall
ALV-4057-M1 #A5	cpy	5.2	92.9	0.1	0.0	1.8	Euhedral to massive chalcopyrite lining internal wall
ALV-4057-M1 #A5	py	0.0	7.0	2.0	0.0	90.9	Massive to fine-grained py aggregates from external wall
ALV-4057-M1 #A5	sph-py	0.1	1.3	45.1	0.0	53.5	Fine-grained sph+py aggregates inside chimney wall
ALV-4057-M1 #A6	cpy	0.9	99.0	0.1	0.0	0.0	Euhedral to massive chalcopyrite lining internal wall
ALV-4057-M1 #A6	py	2.9	0.4	0.2	0.0	96.6	Massive to fine-grained py aggregates from external wall
ALV-4057-M1 #B1	cpy	0.1	99.7	0.2	0.0	0.0	Euhedral to massive chalcopyrite lining internal wall
ALV-4057-M1 #B1	py	0.2	1.0	3.2	0.0	95.5	Massive to fine-grained py aggregates from external wall
K-Vent (Active Fe-Zn-rich chimneys and diffusers)							
ALV-4053-M1 #A1	mar	0.1	2.4	2.4	0.8	94.2	Euhedral mar crystals lining interior of chimney wall
ALV-4053-M1 #A1	py-sph	5.2	1.1	27.2	4.9	61.7	Py-rich grains from external wall of chimney
ALV-4053-M1 #A1	sph-py-ga	2.8	3.0	62.4	9.8	22.0	Sph-rich grains from central part of the chimney wall
ALV-4053-M1 #A2b	mar	0.2	2.5	1.3	0.5	95.4	Euhedral mar crystals lining interior of chimney wall
ALV-4053-M1 #A2b	py-sph	3.5	0.5	14.5	1.3	80.1	Py-rich grains from external wall of chimney
ALV-4053-M1 #A2b	sph-py-ga	0.2	2.0	58.1	14.0	25.8	Sph-rich grains from central part of the chimney wall
ALV-4053-M1 #A2t	py	0.0	0.0	1.9	0.2	97.9	Fine-grained py aggregates from inside of chimney wall
ALV-4053-M1 #A2t	sph-py-ga	0.0	0.8	42.7	6.7	49.8	Fine-grained sph+py aggregates from inside of chimney wall
ALV-4053-M1 #A3	py	0.3	0.0	6.4	0.8	92.4	Fine-grained to collomorph py grains from beehive structure
ALV-4053-M1 #A4	py	0.1	0.0	1.7	0.3	97.9	Fine-grained to massive py grains from beehive structure
ALV-4053-M1 #A4	py-sph	0.2	0.4	29.2	3.4	66.9	Fine-grained sph+py aggregates from beehive structure
ALV-4053-M1 #A5	py	0.1	0.1	5.2	0.7	93.9	Fine-grained to massive py grains from beehive structure
ALV-4053-M1 #A5	py-sph	0.0	0.4	28.8	3.3	67.5	Fine-grained sph+py aggregates from beehive structure
Fe-Zn-rich inactive chimneys							
ALV-4053-M2-a	sph-cpy-ma	0.1	15.0	52.1	0.0	32.9	Mixed fine-grained aggregates of sph and cpy
ALV-4053-M2-a	sph-mar	0.0	1.8	81.4	0.1	16.7	Euhedral sph crystals
ALV-4053-M2-a	mar-sph	0.1	0.8	20.4	0.2	78.5	Fine-grained py/mar from external part of relict chimney wall
ALV-4053-M3	sph-py	0.1	0.9	63.5	0.5	35.0	Fine-grained to euhedral black sph aggregates with minor pyrite
ALV-4053-M3	py-mar	0.2	0.1	7.2	0.2	92.3	Fine-grained py/mar from external part of relict chimney wall
ALV-4057-M2	sph-py-mar	0.3	0.6	70.8	0.0	28.2	Fine-grained to euhedral black sph aggregates with minor pyrite
ALV-4057-M2	py-mar	0.0	0.0	1.7	0.0	98.2	Fine-grained py/mar aggregates
ALV-4059-M3	sph	0.1	0.8	86.6	0.0	12.6	Fine-grained to euhedral black sph aggregates
ALV-4059-M3#1	mar	0.0	0.4	3.2	0.0	96.3	Drust of fine euhedral mar crystals
ALV-4059-M3#2	mar	0.1	0.1	1.2	0.1	98.6	Massive mar grains
ALV-4059-M4#1	py	0.0	0.1	6.0	0.0	93.9	Fine-grained to euhedral py aggregates
ALV-4059-M4#2	py	0.0	0.0	0.3	0.0	99.6	Massive to collomorph py, probably from external rim of relict chimney
Fe-rich massive sulfides							
ALV-4058-M1-a	py	0.0	0.2	0.2	0.0	99.6	Massive to fine-grained py grains
ALV-4058-M1-b#1	py	0.1	5.8	0.2	0.0	94.0	Fine-grained py coating ancient worm tubes
ALV-4058-M1-b#2	py	0.1	0.4	0.3	0.0	99.3	Massive to microcrystalline py
ALV-4059-M2-1	py	0.1	0.7	0.5	0.0	98.7	Drust of fine euhedral py crystals
ALV-4059-M2-2	py	0.1	0.1	0.3	0.0	99.5	Massive py grains

(a) mar: marcasite; py: pyrite; sph: sphalerite; cpy: chalcopyrite; ga: galena; (b) modal abundances of anhydrite calculated using Ca concentration and pure CaSO4 composition; (c) modal abundances of chalcopyrite calculated using Cu concentration and pure CuFeS2 formula; (d) modal abundances of sphalerite calculated using Zn concentration and pure ZnS formula; (e) modal abundances of pyrite-marcasite calculated using Fe concentration after substraction from the contribution of chalcpyrite and sphalerite (containing 10wt% Fe).